Eur. Phys. J. Appl. Phys. **54**, 30001 (2011)
DOI: 10.1051/epjap/2011110017

THE EUROPEAN PHYSICAL JOURNAL APPLIED PHYSICS

Review Article

Turbid medium polarimetry in biomedical imaging and diagnosis

N. Ghosh[a], A. Banerjee, and J. Soni

Department of Physical Sciences, Indian Institute of Science Education and Research (IISER), Kolkata, Mohanpur Campus, PO: BCKV Main Campus Office, Mohanpur 741252, West Bengal, India

Received: 13 January 2011 / Accepted: 3 May 2011
Published online: 14 June 2011 –

Abstract. Studies on polarization properties of scattered light from a random medium like biological tissue have received considerable attention because polarization can be used as an effective tool to discriminate against multiply scattered light (acting as a gating mechanism) and thus can facilitate high resolution imaging through tissue. Further, the polarization properties of scattered light from tissue contain wealth of morphological and functional information of potential biomedical importance. However, in a complex random medium like tissue, numerous complexities due to multiple scattering and simultaneous occurrences of many scattering and polarization events present formidable challenges both in terms of accurate measurements and in terms of analysis of the tissue polarimetry signal. Several studies have therefore been conducted in the recent past to develop appropriate measurement procedures, suitable light propagation models and polarimetry signal analysis methods to overcome these difficulties. In this review, we focus on some of the recent key developments in this area. Specifically, we describe variety of theoretical and experimental tools, illustrated with selected results, aimed at evaluating the prospect of turbid medium polarimetry for both biomedical imaging and diagnosis.

1 Introduction

Optical polarimetry, ever since its discovery, has played important roles in gaining fundamental understanding of the nature of electromagnetic waves and answering some of the key questions related to the physics of light [1]. Traditional polarimetry has also long been pursued for numerous practical applications in various branches of science and technology. Quantification of protein properties in solutions, testing purity of pharmaceutical drugs, remote sensing in meteorology and astronomy, optical stress analysis of structures, and crystallography of biochemical complexes are just a smattering of its diversified uses [2,3]. More recently, the use of polarimetric approaches has also received considerable attention for biological tissue characterization and imaging [4,5]. This is motivated by the fact that polarization can be used as an effective tool to discriminate against multiply scattered light and thus can facilitate high resolution imaging of tissue and its underlying structure [6]. Moreover, the polarization properties of scattered light from tissue contain wealth of morphological, biochemical and functional information (which are otherwise hidden in polarization-blind optical measurements) that can be exploited for non-invasive and quantitative tissue diagnosis [4,5]. For example, the anisotropic organized nature of many tissues stemming from their fibrous structure leads to a specific polarimetry effect, known as linear birefringence (or linear retardance). Muscle fibers and extra-cellular matrix proteins (such as collagen and elastin) possess this kind of fibrous structure and accordingly exhibit optical anisotropy. Changes in this fibrous structure resulting from disease progression or treatment response alter the optical birefringence properties, making this a potentially sensitive probe of tissue status [7,8]. Similarly glucose, present in tissue, exhibits circular birefringence due to its chiral structure. This leads to rotation of the plane of linearly polarized light about the axis of propagation (known as optical rotation or optical activity). Measurements of optical rotation may thus offer an attractive approach for non-invasive monitoring of tissue glucose levels [9].

Despite the promise of the polarimetric approaches for biomedical imaging and diagnosis, in a complex random medium like biological tissue, numerous complexities due to multiple scattering and simultaneous occurrences of many scattering and polarization events confound the traditional polarimetry techniques for accurate measurement and analysis/interpretation of the signal. Multiple scattering causes extensive depolarization, the mechanism of which is controlled by a large number of parameters like density, size, shape and refractive index of complex tissue scattering centers [5]. Further, even if some residual polarization signal can be measured, multiple scattering alters the polarization state in a complex fashion. For optimal performance of the polarization gating approach for imaging through tissue, it is necessary to understand the mechanism of depolarization of light (and the

[a] e-mail: nghosh@iiserkol.ac.in

nature of transfer of residual polarization signal) in tissue and its dependence on the various morphological parameters of tissue. Several studies have therefore been carried out in the recent past to develop experimental strategies for measurement of small polarization-retaining signals in the presence of large depolarized background of multiply scattered light [4,5]. These are supplemented by suitable theoretical treatments (based on radiative transport theory, diffusion theory and Monte Carlo techniques) for modeling polarized light propagation in random medium [10–17]. Numerous studies have also addressed depolarization studies on tissue simulating phantoms (whose constituent scattering and polarization properties are known and user-controlled a priori) to understand the polarization properties of multiply scattered light (and the mechanism of depolarization) in tissue for practical implementation of the polarization gating scheme for tissue imaging [18–22]. Note that for the realization of the polarimetric approaches for quantitative tissue diagnosis also, one needs to develop similar experimental turbid polarimetry systems, theoretical treatments for forward modeling of complex tissue polarimetry events, inverse analysis methods for extraction and quantification of the constituent intrinsic tissue polarimetry characteristics. In this paper, we summarize related research carried out by us and others on exploring turbid medium polarimetry for biomedical imaging and diagnosis.

The paper is organized as follows. In Section 2, we describe the polarized light preliminaries (with an emphasis on Stokes-Mueller formalism) and also define the basic polarization properties. An overview of light transport in turbid medium is provided in Section 3, where the optical transport parameters of tissue are defined and the different light propagation models are described. In Section 4, we describe the experimental schemes for performing polarimetric measurements in tissue-like turbid medium. Basic studies conducted on depolarization of light in turbid medium and representative applications of polarization gated imaging of tissue and tissue-like turbid medium are summarized in Section 5. Section 6 reviews the applications of the polarimetric light scattering (both elastic scattering and fluorescence) approaches for quantitative tissue diagnosis. The paper concludes with a discussion of the other prospective biomedical utility of the turbid polarimetry approaches.

2 Polarized light preliminaries and the basic polarization parameters

As is well known, polarization is a property which arises out of the transverse nature of the electromagnetic (EM) radiation and is related to the orientation of the plane of vibration of its electric field. Mathematically, the propagation of the transverse EM wave (light) in free space can be represented by the transverse components of the associated electric fields as [3,23–25]:

$$E_x(z,t) = E_{0x}\exp[i(\omega t - kz + \delta_x)],$$
$$E_y(z,t) = E_{0y}\exp[i(\omega t - kz + \delta_y)], \quad (1)$$

where E_x and E_y represent the electric fields in the x and y orthogonal directions respectively (z is the propagation direction of the wave), E_{0x} and E_{0y} represent the magnitude of the electric fields, δ_x and δ_y are phases associated with the two transverse electric field components, ω is the frequency of the light, $k = 2\pi/\lambda$, the wave vector (λ is the wavelength of light in free space). The resultant electric field represented as the vector sum of E_x and E_y describes the polarization state of light [3]. Mathematical formalisms for dealing polarized light interaction with any optical system can be broadly classified into two groups: the Jones calculus and the Stokes-Mueller calculus. Jones calculus is a field-based representation and assumes coherent addition of waves [24]. A major drawback of this approach is that it deals with pure polarization states only, thus cannot be used to describe polarization transfer of an optical system that depolarizes an incident polarized light (as is usually encountered in a turbid medium like tissue). This can be encompassed by the Stokes-Mueller formalism, described below.

2.1 Stokes-Mueller formalism

In this formalism, the state of polarization of a beam of light can be represented by four measurable quantities (intensities), when grouped in a 4×1 vector, known as the Stokes vector [3,23–26], introduced by Stokes in 1852. The four Stokes parameters are defined relative to the following six intensity measurements (I) performed with ideal polarizers: I_H, horizontal linear polarizer (0°); I_V, vertical linear polarizer (90°); I_P, 45° linear polarizer; I_M, 135° (−45°) linear polarizer; I_R, right circular polarizer, and I_L, left circular polarizer. The Stokes vector ($\mathbf{S}$) is defined as [23–26]:

$$\mathbf{S} = \begin{bmatrix} I \\ Q \\ U \\ V \end{bmatrix} = \begin{bmatrix} I_H + I_V \\ I_H - I_V \\ I_P - I_M \\ I_R - I_L \end{bmatrix}, \quad (2)$$

where I, Q, U and V are Stokes vector elements. I is the total detected light intensity which corresponds to addition of the two orthogonal component intensities, Q is the difference in intensity between horizontal and vertical polarization states, U is the portion of the intensity that corresponds to the difference between intensities of linear +45° and −45° polarization states, and V is the difference between intensities of right circular and left circular polarization states.

In Stokes formalism, the following polarization parameters of any light beam are defined [3,25–27]:

Net degree of polarization

$$D_{OP} = \frac{\sqrt{Q^2 + U^2 + V^2}}{I}, \quad (3)$$

degree of linear polarization

$$D_{OLP} = \frac{\sqrt{Q^2 + U^2}}{I}, \quad (4)$$

and degree of circular polarization

$$D_{OCP} = \frac{|V|}{I}. \tag{5}$$

Note that the degree of polarization of light should not exceed unity. This therefore imposes the following restriction on the Stokes parameters:

$$\frac{\sqrt{Q^2 + U^2 + V^2}}{I} \leq 1, \tag{6}$$

while the Stokes vectors represent the polarization state of light, Mueller matrix $\mathbf{M}$ (a 4×4 matrix named after its inventor Hans Mueller) represents the polarizing transfer function of any medium in its interaction with polarized light. The two descriptors are linked in the so-called Stokes-Mueller calculus – given a beam with a Stokes vector $\mathbf{S}_i$ impinging on an optical element with a Mueller matrix $\mathbf{M}$, the light output from that element will have its polarization described by a Stokes vector (S_0) as

$$S_0 = MS_i, \tag{7}$$

$$\begin{bmatrix} I_0 \\ Q_0 \\ U_0 \\ V_0 \end{bmatrix} = \begin{bmatrix} m_{11}\ m_{12}\ m_{13}\ m_{14} \\ m_{21}\ m_{22}\ m_{23}\ m_{24} \\ m_{31}\ m_{32}\ m_{33}\ m_{34} \\ m_{41}\ m_{42}\ m_{43}\ m_{44} \end{bmatrix} \begin{bmatrix} I_i \\ Q_i \\ U_i \\ V_i \end{bmatrix}$$

$$= \begin{bmatrix} m_{11}I_i + m_{12}Q_i + m_{13}U_i + m_{14}V_i \\ m_{21}I_i + m_{22}Q_i + m_{23}U_i + m_{24}V \\ m_{31}I_i + m_{32}Q_i + m_{33}U_i + m_{34}V \\ m_{41}I_i + m_{42}Q_i + m_{43}U_i + m_{44}V \end{bmatrix}. \tag{8}$$

Note that the matrix properties enable one to compute the Mueller matrix of an optical system formed by a series of elements, through sequential multiplication of the individual matrices of these elements. If we consider 'n' optical elements, and the light passes through them in order $1, 2, \ldots, n$, then the Mueller matrix of the system can be obtained as

$$M = M_n M_{n-1} \cdots M_2 M_1. \tag{9}$$

The Stokes-Mueller formalism has several advantages. First of all, it can encompass any polarization state of light, whether it is natural, totally or partially polarized (can thus deal with both polarizing and depolarizing optical systems). Secondly, both the Stokes vectors and Mueller matrix can be measured with relative ease using any intensity-measuring instruments, including most polarimeters, radiometers and spectrometers. Moreover, the measured Mueller matrix from any complex system is readily amenable for further analysis in terms of its constituent medium polarimetry characteristics.

The three basic medium polarization properties are *diattenuation*, *retardance* and *depolarization* [26,27]. *Diattenuation* by an optical element arises due to the differential attenuation (absorption and scattering) of orthogonal polarization states (either linear or circular polarization) of the incident light. Accordingly, linear diattenuation is the differential attenuation of two orthogonal linear polarization states (either between 0° and 90° or between 45° and 135°) and circular diattenuation is the differential attenuation of right circular polarized light (RCP) and left circular polarized light (LCP). The Mueller matrix of an ideal diattenuator is generally defined in terms of the magnitude of diattenuation (d) [26,27]. The simplest form of a diattenuator is the ideal polarizer that transforms incident unpolarized light to completely polarized light (magnitude of diattenuation $d = 1$). Nevertheless, many biological molecules (such as amino acids, proteins, nucleic acids) exhibit dichroism or diattenuation, although the effect is rather weak as compared to the other polarization effects.

Retardance is the phase shift between two orthogonal polarizations of the light. Linear retardance (δ) arises due to difference in phase between orthogonal linear polarization states (between 0° and 90° or between +45° and −45°). Circular retardance or optical rotation (ψ) arises due to difference in phase between RCP and LCP. In fact, the functional forms of the Mueller matrices for a linear retarder and a circular retarder in terms of the magnitude of linear retardance δ (and the orientation angle of the pass axis with respect to the horizontal θ) and optical rotation ψ, respectively, are well known [26,27]. In tissue, linear retardance (or birefringence) is a very prominent polarization effect due to the abundance of anisotropic fibrous structures (like muscle fibers and extra-cellular matrix proteins, collagen and elastin). As noted previously, in tissue, circular retardance arises due to the presence of asymmetric chiral molecules, such as glucose, proteins, lipids, etc.

If an incident state is polarized and the exiting state has a degree of polarization less than 1, then the system is known to possess depolarization property. *Depolarization* is usually encountered due to multiple scattering of photons. Incoherent addition of amplitudes and phases of the scattered field results in scrambling of the output polarization state of the emitted light. In a turbid medium like tissue, this is the most common polarimetry effect arising due to strong multiple scattering effects. The Mueller matrix of a depolarizer is generally of diagonal form, its diagonal elements representing depolarization of the different linear (horizontal/vertical, +45°/−45°) and circular (left and right) polarization states [26,27]. The depolarization strength of a medium is usually characterized by the net depolarization coefficient Δ [26,27].

3 Light transport in turbid media such as tissues

Having described the common medium polarimetry characteristics and their corresponding definition in the Stokes-Mueller formalism, we now turn to the complicated issue of forward modeling of light propagation (specifically polarized light) in a complex turbid medium like tissue. Before we address the polarization transfer in such complex system, we shall provide an overview of tissue optics in general, dealing with scattering, absorption and propagation of light in tissue. The basic tissue optic theories will be briefly reviewed in context to turbid polarimetry modeling.

3.1 Introduction to tissue optics

Biological tissue is an optically inhomogeneous, absorbing and turbid medium. Turbidity occurs due to random fluctuations of local refractive index arising from the presence of microscopic inhomogeneities (macromolecules, cell organelles, organized cell structure, extra-cellular matrix, interstitial layers, etc.). Further, these tissue scattering centers vary in size (and shape as well) from few dozen nanometers (sub-cellular structures like mitochondria, ribosomes, lysosomes, Golgi apparatus, etc.) to several tens of micrometers (cells as a whole) [5,28]. Typical refractive index fluctuations in these scattering structures vary from $n_s \sim 1.4$ to 1.5 (the average background refractive index of cytoplasm and interstitial fluid $n_m \sim 1.34$) [28]. Tissue can thus be described as a random continuum of the inhomogeneities of the refractive index with varying spatial scales. In addition to scattering, tissue exhibits significant absorption also. The major contributors of absorption in the ultraviolet (UV) spectral range are DNA and proteins. In the visible and near infrared (NIR) wavelength range, the absorption is dominated by hemoglobin and melanin. Water, the main constituent of all tissues, strongly absorbs beyond about 1.5 μm. For wavelength greater than ∼600 nm and smaller than 1.5 μm, the tissue absorption is however considerably weaker (this wavelength range is known as the *biological window*) [28]. An exact modeling of interaction of light with such complex tissue microstructure in the light of electromagnetic (EM) theory is a formidable task. This will need to identify and incorporate the spatial and temporal distribution of microscopic dielectric structure of tissue and also have to account for strong multiple scattering effects. Such exact modeling is not presently feasible. Despite these difficulties, several researchers have however explored Mie theory, Rayleigh-Gans and Born approximation based simpler light scattering inverse analysis approaches on measured elastic scattering signal (its angular variation or wavelength variation) to extract/quantify microscopic optical properties (size, shape and refractive indices of scatterers) of tissue for its diagnostic applications [29–31]. Note however that the approximations inherent with these models (representation of tissue as an ensemble of homogeneous particles) are valid only for certain types of weakly scattering tissues (such as the blood cells [31]) or for tissues having simpler scattering structures (such as epithelial tissues [29]). For a more general description of light propagation in tissue, the radiative transfer theory (RTT), originally developed by Chandrasekhar [28,32], is often preferred. This is described below.

3.2 Modeling light propagation in tissue and the optical transport parameters

3.2.1 Scalar radiative transfer theory and diffusion approximation

Light propagation in transport theory is described in terms of a macroscopic parameter called *radiance* ($L(r, s, t)$). For this description, tissue is considered to have volumetric scattering and absorption properties. The parameters used to characterize the optical properties of the tissue are, the absorption coefficient (μ_a), single scattering coefficient (μ_s), the total attenuation coefficient ($\mu_t = \mu_a + \mu_s$) and the phase function $p(s, s')$ [28,32]. The linear optical coefficients μ are defined so that $l_a = \mu_a^{-1}$ and $l_s = \mu_s^{-1}$ give the absorption and scattering mean free paths, respectively [28]. The linear optical coefficients are related to the absorption and scattering cross-sections (σ_a and σ_s respectively) by $\mu_a = N\sigma_a$, and $\mu_s = N\sigma_s$. Here N is the particle density and independent scatterer approximation is implicit. The phase function $p(s, s')$ is the probability density function giving the probability of photon to scatter from an initial propagation direction s to a final direction s'. The first moment of the phase function is the average cosine of the scattering angle, denoted by g. It is also referred to as the anisotropy parameter [28,32]. The value of g ranges from -1 to $+1$, where $g = 0$ corresponds to isotropic scattering, $g = +1$ corresponds to ideal forward scattering and $g = -1$ corresponds to ideal backward scattering. Typical values of scattering coefficient μ_s for tissue vary from 5 to 50 mm^{-1} [28]. The values for absorption coefficient μ_a (∼0.01 to 0.1 mm^{-1}) are order of magnitude smaller than μ_s in the biological window (λ = 600 nm–1500 nm, where most of the tissue optical measurements are performed) [28]. Typical values of g for tissues vary from 0.7 to 0.99. Thus tissue is a predominant forward scattering medium. Another parameter frequently used is $\mu_{s'} = \mu_s(1 - g)$ [28]. This is referred to as the reduced scattering coefficient. It defines the probability of photon to be scattered in path length z when the scattering is described by an isotropic function. The use of $\mu_{s'}$ assumes that the reflection and transmission for a slab of tissue with optical parameters μ_a, $\mu_{s'}$ and g are the same as those for the same slab with optical parameters μ_a, $\mu_{s'}$ and $g = 0$ [28,32]. This so-called similarity principle is not exact and holds if the light distribution is studied far enough away from the light source and boundaries, typically at a distance greater than the transport mean free path [$l^* = (\mu_{s'} + \mu_a)^{-1}$] [28,32].

In radiative transfer theory, the time-independent equation for the net change of radiance $L(r, \mathbf{s})$ at position r in the direction of unit vector $\mathbf{s}$ is written as [28,32]

$$s \cdot \nabla L(r, \mathbf{s}) = -(\mu_s + \mu_a)L(r, \mathbf{s}) + \left(\frac{\mu_s}{4\pi}\right) \times \int p(\mathbf{s}, \mathbf{s}')L(r, \mathbf{s}')\mathrm{d}\omega' + \varepsilon(r, \mathbf{s}). \quad (10)$$

Here, the radiance $L(r, \mathbf{s})$ represents the power density per unit solid angle (ω) in direction $\mathbf{s}$ at position r. The first term on the right-hand side represents the depletion of $L(r, \mathbf{s})$ due to absorption and scattering. The second term accounts for increase in radiance due to light scattered from all other directions $\mathbf{s}'$ into the direction $\mathbf{s}$. The last term specifies the contribution to $L(r, \mathbf{s})$ of sources located within the medium.

There are no exact general solutions to the transport equations, making it difficult to use in practical situations.

For weakly absorbing turbid media, in which scattering predominates ($\mu_s \gg \mu_a$), the integro-differential equation of radiation transfer reduces to a simpler photon diffusion equation [32]. The diffusion equation can be solved with appropriate boundary conditions to yield analytical expressions for measurable quantities like diffuse reflectance (R_d), transmittance (T_d) and spatially resolved diffuse reflectance [$R_d(r)$] in terms of the optical transport parameters of tissue [28]. Inverse calculations based on diffusion theory applied to these measured parameters are often used to estimate the optical transport parameters of tissue, namely, μ_a, μ_s, $\mu_{s'}$ and g [28].

3.2.2 Monte Carlo simulation technique

Monte Carlo (MC) simulation technique is a general and robust approach for modeling light transport in random medium [16,28]. In this statistical approach to radiative transfer, the multiple scattering trajectories of individual photons are determined using a random number generator to predict the probability of each scattering event. It is also assumed that scattering events occur independently and exhibit no coherence effects [28]. The position, propagation direction of each photon is initialized and modified as the photon propagates through the scattering medium. The photon propagates in the sample between scattering events a distance sampled from the probability distribution $\exp(-\mu_t z)$. When the photon encounters a scattering event, a scattering plane and angle are statistically sampled based on the scattering phase function. The superposition of many photon paths approaches the actual photon distribution in time and space. This approach has the advantage of being applicable to arbitrary geometries and arbitrary optical properties. The first Monte Carlo models were developed for intensity calculations only and neglected polarization information, the most commonly used being the code of Wang et al. [16]. More recently, a number of implementations have incorporated polarization into their Monte Carlo models [14,17]. These are described later.

3.3 Modeling polarized light propagation through turbid medium

3.3.1 Single scattering modeling based on Mie theory

We shall begin with a simple single scattering theoretical treatment based on Mie theory, developed previously by us [20,21] to understand the mechanism of depolarization of light due to scattering. Mie theory provides exact solution of the vector wave equation for scattering of incident plane wave (light) by any spherical scatterer embedded inside a homogeneous medium [24]. Let us choose the right-handed Cartesian coordinate system with the incident light having an arbitrary polarization (described by Stokes vector $[I\ Q\ U\ V]^{\mathrm{T}}$) propagating in the Z direction and assume that the set of polarizers and the detector are in the X–Y plane, X and Y being the two orthogonal axes. The single scattering Mueller matrix $\mathbf{M}$ relating the Stokes parameters of the incident and the scattered light can be written as [21]

$$(\mathbf{M}) = \left(T_1^{-1}(\phi)\right)\left(T_2^{-1}(\theta)\right)(S(\theta))\,(T_1(\phi))\,, \tag{11}$$

where

$$(T_1(\phi)) = \begin{pmatrix} 1 & 0 & 0 & 0 \\ 0 & \cos 2\phi & \sin 2\phi & 0 \\ 0 & -\sin 2\phi & \cos 2\phi & 0 \\ 0 & 0 & 0 & 1 \end{pmatrix} \quad \text{and}$$

$$(T_2(\phi)) = \begin{pmatrix} \frac{\cos^2\theta+1}{2} & \frac{\cos^2\theta-1}{2} & 0 & 0 \\ \frac{\cos^2\theta-1}{2} & \frac{\cos^2\theta+1}{2} & 0 & 0 \\ 0 & 0 & \pm\cos\theta & 0 \\ 0 & 0 & 0 & \pm\cos\theta \end{pmatrix}.$$

Here, θ is the scattering angle and ϕ is the azimuthal angle. $S(\theta)$ is the scattering matrix defined in the scattering plane [24]. For isotropic spherical scatterer, the general form of $S(\theta)$ is

$$S(\theta) = \begin{bmatrix} S_{11} & S_{12} & 0 & 0 \\ S_{21} & S_{22} & 0 & 0 \\ 0 & 0 & S_{33} & S_{34} \\ 0 & 0 & S_{43} & S_{44} \end{bmatrix}. \tag{12}$$

Note that the symmetry relations for isotropic spherical scatterer allow one to simplify this further, essentially yielding only four independent matrix elements ($S_{11} = S_{22}$, $S_{12} = S_{21}$, $S_{33} = S_{44}$ and $S_{43} = -S_{34}$). On the other hand, for anisotropic scatterers having arbitrary shapes (originating either due to shape anisotropy or intrinsic anisotropy in refractive indices), the form of $S(\theta)$ is far more complex, essentially having non-zero values for all the matrix elements [24].

In equation (11), the transformation matrix $T_1(\phi)$ transforms the laboratory frame Stokes parameters of the incident light wave to the scattering plane. The inverse transformation matrices $T_2^{-1}(\theta)$ and $T_1^{-1}(\phi)$ transform the Stokes parameters of the scattered light from the scattering coordinate to the laboratory coordinate. The symbol (+) in $T_2(\theta)$ corresponds to scattering in forward ($\theta = 0°$–$90°$) and (−) in backward ($\theta = 90°$–$180°$) hemispheres. Summing up contributions for all the values of ϕ (varying from 0 to 2π), the Stokes parameters of the scattered light for incident linearly ($[1\ 1\ 0\ 0]^{\mathrm{T}}$) or circularly ($[1\ 0\ 0\ 1]^{\mathrm{T}}$) polarized light can be obtained as

$$\begin{bmatrix} I_s \\ Q_s \\ U_s \\ V_s \end{bmatrix}_L = \begin{bmatrix} \frac{1}{2}\left[\cos^2\theta\left\{S_{11}(\theta)+S_{12}(\theta)\right\}\right. \\ \quad \left. +\left\{S_{11}(\theta)-S_{12}(\theta)\right\}\right] \\ \frac{1}{4}\left[\cos^2\theta\left\{S_{11}(\theta)+S_{12}(\theta)\right\}\right. \\ \quad \left. +\left\{S_{11}(\theta)-S_{12}(\theta)\right\}\right. \\ \quad\quad \left. +\frac{1}{2}\left|S_{33}(\theta)\cos\theta\right|\right] \\ 0 \\ 0 \end{bmatrix}, \tag{13}$$

$$\begin{bmatrix} I_s \\ Q_s \\ U_s \\ V_s \end{bmatrix}_C = \begin{bmatrix} \frac{1}{2}\left[\cos^2\theta\left\{S_{11}(\theta)+S_{12}(\theta)\right\}\right. \\ \quad \left. +\left\{S_{11}(\theta)-S_{12}(\theta)\right\}\right] \\ 0 \\ 0 \\ \pm\, S_{33}(\theta)\cos\theta \end{bmatrix}, \tag{14}$$

The dependence on scattering angle (θ) for the value of the degree of linear [$P_L(\theta)$] and circular polarization [$P_C(\theta)$] following a single scattering event can be written as [21]

$$P_L = \frac{Q_S(\theta)}{I_S(\theta)}; \quad P_C = \frac{V_S(\theta)}{I_S(\theta)}. \tag{15}$$

The value of the ratio of net degree of polarization after a single scattering event to the initial degrees of linear (P_{OL}) and circular polarization (P_{OC}) can be defined by summing up contribution of all scattering angles (θ varying from 0 to π) [21]

$$P_{OL} = \frac{\int Q_S(\theta)\sin\theta\,\mathrm{d}\theta}{\int I_S(\theta)\sin\theta\,\mathrm{d}\theta}; \quad P_{OC} = \frac{\int V_S(\theta)\sin\theta\,\mathrm{d}\theta}{\int I_S(\theta)\sin\theta\,\mathrm{d}\theta}. \tag{16}$$

The scattering matrix elements $S_{11}(\theta)$, $S_{12}(\theta)$ and $S_{33}(\theta)$ can be computed using Mie theory for a known scatterer (with known radius a, and refractive index n_s) embedded inside a surrounding medium (refractive index n_m). Conventionally in Mie computations, size parameter of scatterer (defined as $X = 2\pi a n_m/\lambda$, λ the wavelength) and the relative refractive index ($m = n_s/n_m$) are taken as input parameters for generating the angle dependent scattering matrix elements [24]. Thus computed scattering matrix elements can be used to generate the values for the polarization parameters defined in equations (15) and (16). Note that for quantitative description of actual depolarization of polarized light in a turbid medium, one would need to incorporate degree of polarization after individual scattering event (Eq. (15)) in multiple scattering models such as polarization-sensitive Monte Carlo simulations (described later). In contrast, the polarization parameters defined in equations (15) and (16) typically neglect the complexities of multiple scattering and are defined by averaging out contributions of light scattered at different angles q; these therefore describe the net rate of depolarization per scattering in a turbid medium (depolarization strength of the medium in an averaged sense). However, as we shall see later, these single scattering parameters, approximate though, provide useful insight into the mechanisms of depolarization of light in turbid medium, help in optimizing the polarization scheme for imaging and can also be used to explain some of the rather intriguing depolarization behavior of light in actual tissues.

3.3.2 Vector radiative transfer equation

The scalar radiative transport theory, described previously, typically neglects polarization information. The polarization information can be incorporated by replacing the specific intensity term ($L(r,s,t)$) in the scalar radiative transfer equation (Eq. (10)) by the Stokes vector ($\mathbf{S}$) and by using vector representation of other related parameters. Thus obtained radiative transfer equation is known as the vector radiative transfer equation (VRTE) and can be written as [5,32]

$$\frac{\mathrm{d}S(\vec{r},\vartheta,\varphi)}{\mathrm{d}\tau(\vec{r})} = -S(\vec{r},\vartheta,\varphi) + \frac{\Lambda(\vec{r})}{4\pi}\int_{-1}^{+1}\mathrm{d}(\cos\vartheta') \times \int_0^{2\pi}\mathrm{d}\varphi'\,\vec{Z}(\vec{r},\vartheta,\vartheta',\varphi-\varphi')S(\vec{r},\vartheta,\varphi). \tag{17}$$

Here, $S(\vec{r},\vartheta,\varphi)$ is the Stokes vector; $\vec{r}$ is the position vector; ϑ,φ are angles characterizing the incident direction, the polar and the azimuth angles; $\mathrm{d}\tau(\vec{r}) = \rho(\vec{r})\sigma_{\mathrm{ext}}(\vec{r})\mathrm{d}s$ is the optical thickness; ρ is the local particle number density and σ_{ext} is the local ensemble-averaged extinction coefficient; $\mathrm{d}s$ is the pathlength element.

$\lambda = \frac{\sigma_s}{\sigma_{\mathrm{ext}}}$ is the single scattering albedo [32]; ϑ',φ' are angles characterizing the scattered light direction. $\vec{Z}(\vec{r},\vartheta,\vartheta',\varphi-\varphi')$ is the normalized phase matrix, relating the Stokes vector of the incident and scattered light, specified relative to their respective meridional planes (similar in spirit to $\mathbf{M}$ defined in Eq. (11)).

As for the case of scalar radiative transfer equation, the solution for VRTE for real systems is rather complex. A wide range of analytical and numerical techniques have been developed to solve VRTE, namely, the small angle approximation method, the transfer matrix method, the singular eigenfunction method, the adding-doubling method, the discrete ordinates method, the successive orders methods and the invariant embedding method [28,32]. Unfortunately, these are often too slow and insufficiently flexible to incorporate the necessary boundary conditions for arbitrary geometries and arbitrary optical properties as desirable in case of tissue. The polarization-sensitive Monte Carlo (PSMC) techniques are thus more widely used for forward modeling polarized light transport in turbid medium and are considered the "gold standard" of tissue polarimetry modeling.

3.3.3 Polarization-sensitive Monte Carlo models

Similar to conventional Monte Carlo modeling, in PSMC also it is assumed that scattering events occur independently and have no coherence effects [28]. A flowchart for PSMC model is shown in Figure 1. In addition to modification/incorporation of the position and propagation direction of each photon (while propagating through the turbid medium), polarization information is incorporated by keeping track of the Stokes vectors of propagating photon packets. When the photon encounters a scattering event, a scattering plane and angle are statistically sampled based on the polarization state of the photon and the Mueller matrix of the scatterer. The photon's reference frame is first expressed in the scattering plane and then transformed to the laboratory (experimentally observable) frame through multiplication by appropriate rotation matrices and the Mueller matrix calculated through Mie scattering theory (similar to $\mathbf{M}$ defined in Eq. (11)) [17,28]. Upon encountering an interface (either an internal one, representing tissue layers of different optical properties,

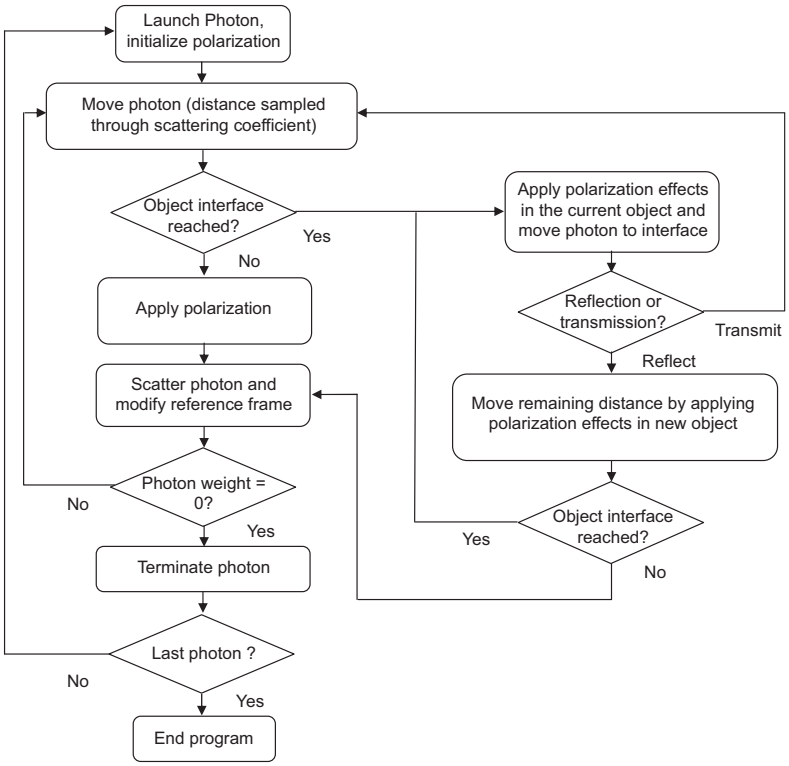

Fig. 1. A flow chart for polarization-sensitive Monte Carlo model. (Adapted from Ref. [33].)

or an external one, representing external tissue boundary), the probability of either reflection or transmission is calculated using Fresnel coefficients. As no coherence effects are considered, the final Stokes vector for light exiting the sample in a particular direction is computed as the sum of all the appropriate directional photon sub-populations.

Although several PSMC models have been developed based on the above approach, a general problem is encountered in simulating all the polarization effects in tissue. This is primarily due to the inherent difficulty in formulating *simultaneous* polarization effects (in tissue these include optical activity, linear birefringence and depolarization), especially in the presence of multiple scattering. Matrix multiplication of the Mueller matrices for individual polarization effects is not commutative ($\mathbf{M}_A\mathbf{M}_B \neq \mathbf{M}_B\mathbf{M}_A$), thus, different orders in which these effects are applied will have different effects on the polarization. This problem has been addressed by Wood et al. [17]. In their PSMC model, simultaneous polarization effects were incorporated through the use of the so-called N-matrix formalism [17,34]. Briefly, in this approach, the matrix of the sample is represented as an exponential function of a sum of matrices, where each matrix in the sum corresponds to a single optical polarization effect. The issue of ordering of non-commutative matrices is overcome as matrix addition is always commutative. Once converted to a Mueller matrix, this matrix is applied to the photons as they propagate between scattering events. This approach enabled the combination of any number of simultaneously occurring polarizing effects. Finally, as shown in Figure 1, the scattering histories of a large number of photon packets (typically 10^7–10^9 photons required to generate statistically acceptable results) are tracked as they propagate through the medium and are summed to yield the macroscopic parameters of practical interest (Stokes vectors, Mueller matrices, pathlength distributions, polarization statistics from different scattering histories, etc.).

Till date, the PSMC model of Wood et al. [17] appears to be the most accurate Monte Carlo tissue polarimetry model. In fact, the ability of this PSMC model to simulate *simultaneous* polarization effects in the presence of multiple scattering was experimentally validated by them on solid polyacrylamide phantoms exhibiting simultaneous linear birefringence, optical activity, and depolarization (multiple scattering) [17].

3.3.4 Analytical modeling of depolarization of multiply scattered waves

There has been considerable interest in developing simpler analytical formulation for depolarization of multiply scattered waves in random medium. Various approaches using photon diffusion formalisms, random walk models, maximum entropy principles have been used to derive analytical relationships between the degree of polarization (either linear or circular) of forward-scattered or back-scattered light from a turbid medium with the optical transport parameters of the medium [10–15]. Such physical modeling is certainly important in gaining physical insight into the mechanism of depolarization of multiply scattered waves in a turbid medium.

Pioneering work in this direction was carried out by Bicout et al. [11]. They envisioned that depolarization of light by multiple scattering can be connected to a process of entropy production [10,11]. Based on the so-called maximum entropy principle, it was shown that the single path (photon undergoing successive scattering events) degree of polarization decays exponentially with increasing number of scattering events (n) [10]. This approximation has been confirmed later by various experimental studies [11]. For a medium comprised of a collection of non-absorbing, optically inactive, spatially uncorrelated, spherical particles whose size is much smaller compared to wavelength (radius $a \ll \lambda$, anisotropy parameter $g \sim 0$, the so-called Rayleigh regime), expression for single path degree of linear and circular polarization (for incident linearly or circularly polarized light respectively) was derived as [11]

$$P_L(n) = \frac{3}{2}\exp[-n(l/\xi_l)] \quad \text{and} \quad P_C(n) = \frac{3}{2}\exp[-n(l/\xi_c)]. \tag{18}$$

Here, $l = \mu_s^{-1}$ is the scattering mean free path, and the parameters ξ_l and ξ_c are known as characteristic length scale of depolarization of incident linearly and circularly polarized light respectively. For a medium comprised of ensemble of Rayleigh scatterers ($a \ll \lambda$, $g \sim 0$), the values for ξ_l and ξ_c were determined to be

$$\xi_l = \frac{l}{\ln(10/7)} \quad \text{and} \quad \xi_c = \frac{l}{\ln(2)} \quad \text{with } \xi_l \cong 2\xi_c. \tag{19}$$

The dependence of depolarization on size parameter (X) for larger sized scatterers ($a \geq \lambda$, $g \geq 0.7$, Mie regime) was also addressed by Bicout et al. by incorporating Mie theory in the model [11]. Thus obtained size parameter dependence of ξ_l and ξ_c was found to be in excellent agreement with experimental depolarization studies conducted on scattering media comprised of spherical scatterers having varying sizes, and also with the corresponding polarization-sensitive Monte Carlo simulations of similar multiply scattering media [11]. The dependence of ξ on size parameter of scatterer (or anisotropy parameter g) has been studied by many other researchers also. Rojas-Ochoa et al. [15] used an extended photon diffusion approximation combined with experimental measurements using diffusing wave spectroscopy (measurements of intensity fluctuations of light scattered from turbid media) for deriving empirical relationships between ξ and g. Kim and Moscoso [13] and Xu and Alfano [35] have also studied the similar dependence using the theory of radiative transfer and random walk models respectively. The essence of these studies can be summarized through the following two empirical equations [15,35]:

$$\frac{\xi_l}{l} = \frac{\frac{1}{\ln(10/7)} - 2.5g}{(1-g)} \quad \text{and} \quad \frac{\xi_c}{l} = \frac{\frac{1}{\ln 2}}{(1-g)}. \tag{20}$$

Note that the degree of residual polarization of multiply scattered optical field at an arbitrary chosen detection point can be determined by averaging (or weighing) the single path degree of polarization (Eq. (18)) over the pathlength distribution function ($\rho(n)$) as

$$P_{L,C} = \frac{\int_0^\infty P_{L,C}(n)\rho(n)\mathrm{d}n}{\int_0^\infty \rho(n)\mathrm{d}n}. \tag{21}$$

Analytical expression for $\rho(n)$ in various geometries can be obtained from the solution of photon diffusion equation [28,32]. In fact, Bicout et al. [11] derived a closed form analytical expression for surviving degree of polarization of light transmitting through a slab of scattering medium by incorporating the diffusion theory-based expression for $\rho(n)$ in equation (21). Similar expressions for residual degree of polarization of back-scattered (a geometry that is convenient for many practical applications) light have also been obtained by others [5,36]. For example, Zymniakov et al. used path integral approach to derive expression for residual degree of polarization (P_L) of linearly polarized light back-scattered from turbid medium [36]. In this approach, the single path degree of polarization [$P_L(s), s = nl$, the pathlength] was averaged over the ensemble of partial components of the scattered optical fields characterized by the pathlength density distribution function [$\rho(s)$], to yield the following expression for P_L of back-scattered light:

$$P_L \cong \frac{3}{2}\exp\left[-\gamma\sqrt{\frac{3l^*}{\xi l}}\right]. \tag{22}$$

Here l^* is the transport mean free path and γ is the correlation decay parameter with its value ranging from 1.5 to 3 [5].

The effect of medium absorption on P_L has also been incorporated by modifying [$\rho(s)$] to take into account finite absorption (by multiplying it with a factor $\exp[-\mu_a s]$) [5]. Accordingly, the expression for P_L in absorbing turbid medium takes the form

$$P_L \cong \frac{3}{2}\exp\left[-\gamma\left\{\sqrt{\frac{3l^*(1+\mu_a\xi_l)}{\xi_l}}\right\} - \sqrt{3l^*\mu_a}\right]. \tag{23}$$

An interesting feature that can be noted from equations (19) and (20) is that for a medium comprised of Rayleigh scatterers ($a \ll \lambda$, $g \sim 0$), depolarization of circularly polarized light should be stronger than linearly polarized light ($\xi_l > \xi_c$). The reverse should be the case ($\xi_l < \xi_c$) for media comprised of larger scatterers ($a \geq \lambda$, $g \geq 0.7$, Mie regime). It is also pertinent to note here that the single scattering depolarization factors (P_{OL} and P_{OC}) defined in equation (16) and the characteristic depolarization lengths (ξ_l and ξ_c) are closely related. While the former is defined based on power-law decay ($P^n_{OL/OC}$) of degree of polarization, the latter is defined based on an exponential decay. These parameters may thus be related through the following analogy:

$$\frac{\xi_{l,c}}{l} = \frac{1}{\ln\left(\frac{1}{P_{OL,OC}}\right)}. \tag{24}$$

4 Experimental turbid medium polarimetry systems

Polarimeters can be regarded as optical instruments used for the determination of polarization characteristics of light and the sample. Based on this definition, experimental polarimetry systems can be broadly classified into two categories: (i) the light measuring polarimeters and (ii) the sample measuring polarimeters. The light measuring polarimeters (Stokes polarimeters) determine the polarization state of a light beam, by measuring the four Stokes parameters (Stokes vector $[I\ Q\ U\ V]^{\mathrm{T}}$). In contrast, the sample measuring polarimeters (Mueller matrix polarimeters) aim to determine the complete 4×4 Mueller matrix. Here, we shall discuss some common strategies employed in these polarimeters, specifically for turbid medium investigation.

4.1 Light measuring polarimeters

The classical method for determination of the four Stokes parameters involves six intensity measurements (I) according to equation (2) – I_H, horizontal linear polarizer (0°); I_V, vertical linear polarizer (90°); I_P, 45° linear polarizer; I_M, 135° (−45°) linear polarizer; I_R, right circular polarizer, and I_L, left circular polarizer. A schematic of experimental set-up for this classical method is shown in Figure 2. Note that for Stokes parameters measurement, one is mainly concerned about the polarization state analyzer (PSA) part of the set-up. The polarization state generator (PSG) is used to generate one particular incident polarization state (either linear or circular). As shown in the figure, the PSA usually comprises of a linear polarizer (P_2) and a waveplate (WP_2) for performing the required six intensity measurements. In this case, the waveplate is a quarter wave retarder. Note that the four intensity measurements involving linear polarization states (I_H, I_V, I_P, I_M) are performed by removing the quarter waveplate, whereas the quarter waveplate is inserted for the two remaining intensity measurements involving circular polarization states (I_R, I_L). Collett [37] proposed a method involving just four measurements, based on the property ($I_H + I_V = I_P + I_M = I_L + I_R$). Briefly, a circular polarizer (the PSA here) consists of a linear polarizer whose transmission axis is set at +45° with respect to the horizontal direction followed by a quarter waveplate with its fast axis parallel to the horizontal direction. Three sets of intensities $[I_C(\alpha)]$ are detected by changing the angle (α) of this circular polarizer to 0°, 45° and 90° with respect to the horizontal axis. The combined polarizer is then flipped to the other side and the final intensity measurement $[I_L(\alpha)]$ is made by setting α at 0°. The four Stokes parameters can be obtained from the measured intensities as

$$\begin{bmatrix} I \\ Q \\ U \\ V \end{bmatrix} = \begin{bmatrix} I_c(0°) + I_c(90°) \\ I - 2I_c(45°) \\ Ic(0°) - Ic(90°) \\ -I + 2I_L(0°) \end{bmatrix}. \tag{25}$$

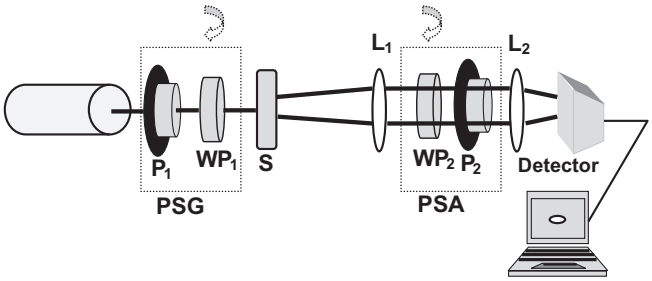

Fig. 2. A schematic of the experimental polarimetry system. P_1, P_2 linear polarizers; WP_1, WP_2 quarter waveplates; L_1 L_2 lenses respectively. Note that for Stokes parameter measurement, the polarization state analyzer (PSA) part of the set-up is generally used, with the analyzing waveplate WP_2 being a quarter wave retarder. For dual rotating retarder Mueller matrix polarimetry, both the polarization state generator (PSG) and the polarization state analyzer (PSA) components of the set-up are used. Here, WP_1, WP_2 are rotating waveplates with linear retardations δ_1 and δ_2 and rotation speeds ω_1 and ω_2 respectively.

This particular scheme of measurement has been employed by us and many others to measure Stokes parameters of light transmitted (or back-scattered) from tissue and tissue-like turbid medium [20–22]. Note that this method does not employ any polarization modulation scheme. However, to obtain polarization signals in strongly depolarizing scattering media such as tissues, one may need to employ polarization modulation and synchronous detection schemes for improving the sensitivity of the measurement procedure. This follows because multiple scattering leads to depolarization of light, creating a large depolarized source of noise that hinders the detection of the small residual polarization-retaining signal. Various experimental strategies based on polarization modulation and synchronous detection schemes have therefore been proposed [26,38]. Generally in this approach, the polarization state analyzer contains a polarization modulator, a rapidly changing (with time) polarization element. The output of PSA is thus a rapidly fluctuating intensity (oscillating at a frequency of $\omega_p = 2\pi f_p$, set by the modulator) on which the polarization information is coded. The polarization information is then extracted by synchronously detecting the time-varying signal at the fundamental modulation frequency and its different harmonics. Various types of resonant devices like the electro-optical modulator, the magneto-optical modulator and the photoelastic modulators (PEMs) have been employed for polarization modulation. Among these the PEMs have been the most widely used [34,39]. The synchronous detection of the modulated signal can be conveniently done by using a lock-in amplifier [39].

4.2 Sample measuring polarimeters

As noted previously, the sample measuring polarimeters measure the complete 4×4 Mueller matrix of the sample. For Mueller matrix measurements also, both dc measurement (involving sequential measurement) and

Table 1. Construction of Mueller matrix from 16 combinations of intensity measurements. The first and the second letters in the intensity measurements correspond to incident and detection polarization states respectively. The different polarization states are: H = Horizontal, V = Vertical, $P = +45^\circ$ and R = Right circular polarization.

$M_{11} = HH + HV + VH + VV$	$M_{12} = HH + HV - VH - VV$	$M_{13} = 2PH + 2PV - M_{11}$	$M_{14} = 2RH + 2RV - M_{11}$
$M_{21} = HH - HV + VH - VV$	$M_{22} = HH - HV - VH + VV$	$M_{23} = 2PH - 2PV - M_{21}$	$M_{24} = 2RH + 2RV - M_{21}$
$M_{31} = 2HP + 2VP - M_{11}$	$M_{32} = 2HP - 2VP - M_{21}$	$M_{33} = 4PP - 2PH - 2PV - M_{31}$	$M_{34} = 4RP - 2RH - 2RV - M_{31}$
$M_{41} = 2HR + 2VR - M_{11}$	$M_{42} = 2HR - 2VR - M_{21}$	$M_{43} = 4PR - 2PH - 2PV - M_{41}$	$M_{44} = 4RR - 2RH - 2RV - M_{42}$

modulation-based measurement procedures have been employed. The former approach involves sequential measurements with different combinations of source polarizers and detection analyzers. Because a general 4 × 4 Mueller matrix has 16 independent elements, at least 16 independent measurements are required for the construction of Mueller matrix [26,40]. The process for construction of Mueller matrix from 16 such combination of intensity measurements is listed in Table 1 [40]. In Table 1, the first and the second letters (H, V, P, R) in the intensity measurements correspond to incident and detection polarization states respectively. Note that methods involving a greater number of polarization measurements such as 36 polarization measurements and 49 polarization measurements have also been explored for the construction of Mueller matrix. As number of measurements increases, the accuracy also increases because in the methods with lesser measurements, error in the measurements of one element of the Mueller matrix propagates to cause further errors in other elements (which are indirectly obtained).

Various polarization modulation schemes have also been employed for simultaneous determination of all the 16 Mueller matrix elements. As for the case of Stokes polarimeters, here also various optical elements like liquid crystal variable retarders, photoelastic modulators (PEMs), etc., have been used for modulating either the polarization state of light that is incident on the sample (by keeping the polarization modulator between the source and the sample) or the sample-emerging light (by placing the polarization modulator between the sample and the detector) or both [38]. Among the various modulation-based Mueller matrix polarimeters, the dual rotating retarder polarimeter, originally proposed by Azzam [41] and first implemented by Goldstein [42], has been widely used in turbid polarimetry investigations. A schematic of the setup is shown in Figure 2. Light from the source first passes through a fixed linear polarizer and then through a rotating linear retarder (retardation δ_1) with angular speed ω_1 to generate polarization modulation of the incident state. The analyzing optics contains another rotating retarder (retardation δ_2, synchronously rotating at angular speed ω_2) and a fixed linear polarizer. In the original configuration of Azzam, the axis of the polarizers was parallel, the retarders were quarter waveplates ($\delta_1 = \delta_2 = \pi/2$) and these were rotated at angular speeds of $\omega_1 = \omega$ and $\omega_2 = 5\omega$ respectively [41]. This five to one ratio encodes all 16 Mueller matrix elements onto the amplitude and phases of 12 frequencies in the detected intensity signal. The detected signal is Fourier analyzed and the Mueller matrix elements are constructed from the Fourier coefficients [26,41]. A more general polarimetry data analysis approach based on this dual rotating retarder method however employs arbitrary values for linear retardations (δ_1 and δ_2), rotation speed ratios (ω_1 /ω_2) and axis of the linear polarizers, depending upon which elements (rows/columns) of Mueller matrix are given a priority [26].

Apart from the dual rotating retarder method, various other modulation techniques employing dual PEM or a combination of liquid crystal variable retarders and PEM for modulating the polarization state generator (PSG) and polarization state analyzer (PSA) have also been employed. The Mueller matrix polarimeters based on liquid crystal variable retarders have the added advantage of enabling large area polarimetry imaging with high sensitivity and precision. For details of the designing and working principles of these polarimeters, the reader is referred to references [26,38,43,44]. Another important development in Mueller matrix polarimetry is the Snapshot Mueller matrix polarimeter [45]. Briefly, in this approach, wavelength polarization coding and decoding is exploited for instantaneous measurement of all the 16 Mueller matrix elements. The wavelength coded several polarization states are generated with a broadband light source, using two birefringent retarders and a linear polarizer. The wavelength decoding is performed using a similar combination of birefringent retarders and a linear polarizer. The thickness of the retarders in the coding (PSG) and decoding (PSA) systems is optimized to generate and analyze sufficient number of polarization states; the resulting spectral signal recorded using a spectrometer is Fourier analyzed to yield all the 16 Mueller matrix elements.

5 Polarization gated imaging of tissue and tissue-like turbid media: selected results and trends

Development of optical techniques for biomedical imaging is an actively pursued area. However, a major difficulty encountered in using optical techniques for medical imaging is the fact that multiple scattering within tissue leads to loss of directionality that results in image blurring. Several experimental approaches such as time gating, spatial filtering, coherence gating and polarization gating have therefore been explored for extracting the unscattered (ballistic photons) or weakly scattered (snake) photons from the diffused (multiply scattered) photons for

imaging [46]. Polarization gating has received particular attention because of the relative simplicity of instrumentation, making this a potential tool amenable for clinical use. This approach exploits the fact that multiply scattered light gets depolarized and therefore by detecting the polarized component of light scattered from tissue one can filter out the multiply scattered (image blurring) photons and extract the weakly scattered or un-scattered (image bearing) photons and thus can improve resolution and contrast of image [6]. However, for optimal performance of this approach in tissue imaging, it is important to understand the mechanism of depolarization and its dependence on the different morphological parameters of tissue (like the density, size and its distribution, shape and refractive index of the tissue scatterers). A number of experimental studies have therefore investigated this aspect. We shall briefly summarize these (with illustrative examples) and discuss their implications for polarimetric tissue imaging.

5.1 Depolarization of light in turbid medium and the efficiency of polarization scheme for imaging through tissue

Since it is difficult to quantify the morphological parameters of a complex system like tissue, in most of the experimental depolarization studies, the individual influence of these morphological parameters has been systematically investigated on well-characterized tissue simulating phantoms [6,18–22]. Suspension of Intralipid or aqueous suspension of polystyrene microspheres has usually been used to prepare tissue phantoms for polarimetric studies [18–22]. The usual approach has been to use a chosen size of scatterers that would give a value of anisotropy parameter (g) comparable to that of tissue. The concentration of scatterers is then adjusted to yield the value of optical thickness ($\tau = \mu_s \times t, \mu_s$ is the scattering coefficient and t is the physical thickness) or reduced optical thickness ($\tau' = \mu_{s'} \times t, \mu_{s'}$ is the reduced scattering coefficient) comparable to that of actual tissue. Pioneering studies in this direction were carried out by Schmitt et al. [6]. Using Monte Carlo simulation of polarized light transport and by carrying out experimental studies on scattering samples prepared using monodisperse spherical scatterers, they investigated the possibility of utilizing degree of polarization to discriminate against multiply scattered light. Motivated by the encouraging results of this pioneering study, several theoretical [11–15,35,36] and experimental investigations [18–22,47,48] have been carried out to develop optimal polarization scheme for imaging through tissue. We shall summarize these with representative results.

Figure 3a and 3b shows measured degree of polarization as a function of optical thickness τ from samples prepared using aqueous (refractive index $n_m = 1.33$) suspension of 0.11 μm diameter polystyrene (refractive index $n_s = 1.59$) microspheres (anisotropy parameter $g = 0.09$, size parameter $X = 0.72$ at 632.8 nm) and from samples having 1.08 μm diameter polystyrene microspheres ($g = 0.92$ and $X = 7.13$) as scatterers respectively. The degree of polarizations (both linear and circular) was determined by measuring the Stokes parameters $[I\ Q\ U\ V]^{\mathrm{T}}$ of the transmitted light using the experimental scheme described in Section 4.1 (Fig. 2a, and Eqs. (4) and (5)) [22]. Note that the scattering samples prepared using 0.11 μm diameter and 1.08 μm diameter microspheres can be treated as isotropic ($g \leq 0.2$, radius $a \ll \lambda$, $X \leq 2$) and anisotropic scattering ($g \geq 0.7$, $a \geq \lambda$, $X > 2$) samples respectively. The most pertinent feature that can be noticed is that while for the isotropic scattering samples degree of circular polarization falls sharper than degree of linear polarization with increasing value of τ, the reverse is the case for anisotropic scattering samples. Moreover, the overall strength of depolarization is considerably weaker for the anisotropic scattering samples. These results are in qualitative agreement with the theoretical predictions of equation (16) (Sect. 3.3.2) and equation (20) (Sect. 3.3.4). These are shown in Figure 4, where the computed values (using Eq. (16)) for the net rate of depolarization per scattering event for incident linearly (P_{OL}) and circularly (P_{OC}) polarized light as a function of size parameter of scatterer (X) are shown [21]. The corresponding variations of characteristic length scale of depolarization for incident linearly and circularly polarized light (ξ_l and ξ_c computed using Eqs. (20) and (24)) are also shown in the inset of the figure. As the value for X increases, the value for the factors P_{OL} and P_{OC} (as well as ξ_l and ξ_c) increases indicating weaker depolarization for larger values of X. Further, while the depolarization is significantly more for incident circularly polarized light than linearly polarized light at smaller values of size parameter of scatterer ($X < 2, g \leq 0.2$), the reverse is the case for larger size parameter of scatterer ($X > 2$, $g \geq 0.7$). Similar trends have been reported in many experimental and theoretical investigations including those by Bicout et al. [11], Schmitt et al. [6] and Gorodnichev et al. [12].

The reduction in the rate of depolarization with increasing X is expected because the larger the value for X (larger value of g) more predominant is forward scattering and hence lesser should be the depolarization [6,11,12]. The reason for the difference in relative behavior of depolarization of linearly and circularly polarized light was shown to arise due to the different mechanism of depolarization of the two different polarization states [12,21]. The depolarization of incident linearly polarized light occurs primarily due to the randomization of the direction of the incident field vector as a result of multiple scattering [12,13,21]. On the other hand depolarization of circularly polarized light occurs both due to the randomization of the field vector's direction and randomization of the helicity [12,13]. It should be noted that while exact backscattering does not affect linear polarization, it can flip the helicity of the circular polarization state resulting in larger depolarization. While for the scatterers with smaller size parameter the helicity flips at $\theta \sim 90°$, for larger sized scatterers, it is preserved up to a much larger value of θ [20]. Since scatterer with smaller size scatters light isotropically where forward scattering and backscattering occurs in the same footing, the depolarization of circularly polarized light is more pronounced for isotropic scattering samples ($X < 2$, $g \leq 0.2$). As the scatterer size increases, the additional cause of depolarization of

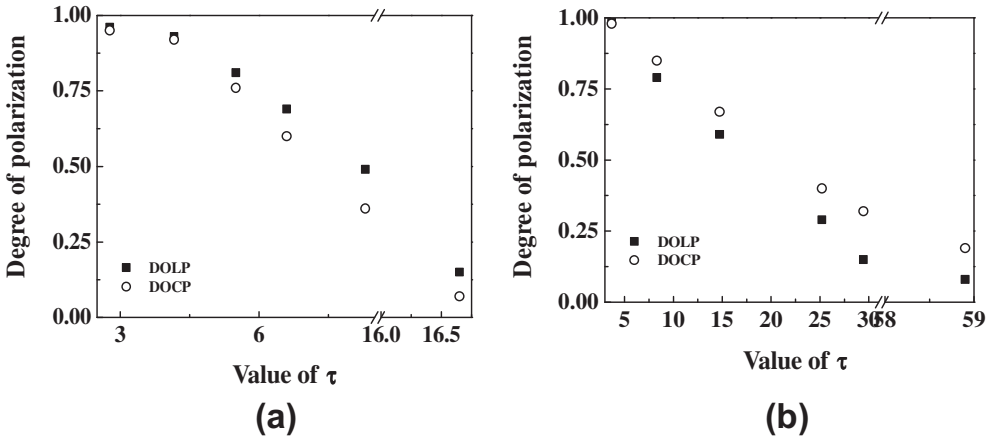

Fig. 3. Experimentally measured degrees of linear (D_{OLP}, ■) and circular (D_{OCP}, ○) polarization as a function of optical thickness τ from samples prepared using aqueous (refractive index $n_m = 1.33$) suspension of (a) 0.11 μm diameter polystyrene (refractive index $n_s = 1.59$) microspheres (anisotropy parameter $g = 0.09$, size parameter $X = 0.72$ at 632.8 nm) and (b) from samples having 1.08 μm diameter polystyrene microspheres ($g = 0.92$ and $X = 7.13$) as scatterers. (Adapted from Ref. [22].)

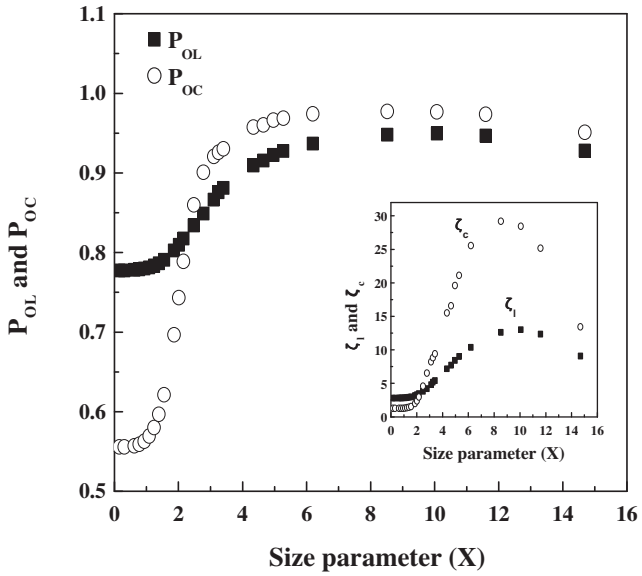

Fig. 4. The computed values for the net rate of depolarization per scattering event for incident linearly (P_{OL}, ■) and circularly (P_{OC}, ○) polarized light as a function of size parameter of scatterer (X). The inset shows corresponding variations for characteristic length scale of depolarization for incident linearly (ξ_l) and circularly (ξ_c) polarized light. (Adapted from Ref. [21].)

circularly polarized light i.e., the flipping of helicity also gets reduced, resulting in weaker depolarization of circularly polarized light for anisotropic scattering samples ($X > 2$, $g \geq 0.7$).

Note that the relative efficiency of the different polarization schemes for filtering out multiply scattered light is not solely determined by the net depolarization strength of the medium. It is also controlled by the angular (or spatial) distribution of degree of polarization of light propagating through the turbid medium. This has been studied either theoretically by using polarization-sensitive Monte Carlo simulations [14] or experimentally by recording the spatial distribution of degree of polarization of diffusely transmitted (or reflected) light in the detector (e.g., in CCD pixels) [18,20,22]. The spatial distribution of degree of polarization aimed at evaluating the efficiency of polarization gated imaging (illustrated below with selected results) is known as polarization spread function (PSF).

Figures 5a and 5b show the experimentally measured spatial distribution of the degree of linear and circular polarization of light transmitted through isotropic scattering samples ($g = 0.09$) prepared using 0.11 μm diameter polystyrene microspheres (optical thickness $\tau = 8.3$) and anisotropic scattering samples ($g = 0.92$) prepared using 1.08 μm diameter polystyrene microspheres ($\tau = 8.3$) [22]. The PSFs for either linear or circular polarizations show sharper profile with a distinct peak around the beam center (ballistic beam direction) for the isotropic scattering sample, the profile for degree of circular polarization being sharper than that for degree of linear polarization. In contrast, for the anisotropic scattering sample, the overall PSFs are flat, the profile for degree of linear polarization being marginally sharper than the degree of circular polarization. The observed distinct peaks in the spatial spread of degree of polarization of isotropic scattering samples arise because for these samples, the transmitted light located at the beam center is primarily contributed by un-scattered or weakly scattered (scattered at narrow angle) photons that maintain its initial state of polarization. In contrast, the transmitted light located far away from the propagation axis is dominated by multiply scattered photons that suffer series of large angle scattering events and are therefore depolarized to a greater extent [6,18,22]. The sharpness of the PSF depends upon the

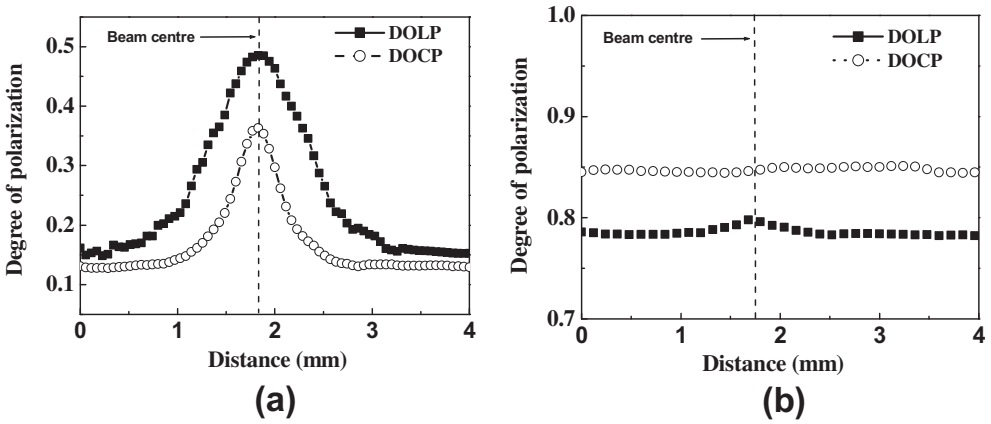

Fig. 5. Experimentally measured spatial distribution of the degrees of linear (D_{OLP}, ■) and circular (D_{OCP}, ○) polarization of light transmitted through (a) isotropic scattering samples ($g = 0.09$) prepared using 0.11 μm diameter polystyrene microspheres (optical thickness $\tau = 8.3$) and (b) anisotropic scattering samples ($g = 0.92$) prepared using 1.08 μm diameter polystyrene microspheres ($\tau = 8.3$). (Adapted from Ref. [22].)

rate at which the value of degree of polarization decreases with increasing scattering angle (θ) after individual scattering events (the single scattering parameters $P_L(\theta)$ and $P_C(\theta)$ defined in Eq. (15) of Sect. 3.3.1). In fact, the computed angular variations of $P_L(\theta)$ and $P_C(\theta)$ were found to corroborate well with these experimental trends (not shown here) [20]. Nevertheless, in such situation (for isotropic scattering medium, $X < 2$, $g \leq 0.2$), the degree of polarization (specifically circular polarization) can be used as an effective scheme to filter out the multiply scattered photons from the weakly scattered photons. On the other hand, the relative flatter profiles for PSF in anisotropic scattering medium ($X > 2$, $g \geq 0.7$) indicate that the polarization scheme for imaging would in general be less efficient as compared to that in isotropic scattering medium. Further linear polarization gating should be marginally superior scheme for imaging in anisotropic scattering medium. Note however since degree of circular polarization is preserved up to a larger value of τ (Fig. 3b), the limiting depth of imaging should be greater with circular polarization gating.

It should be mentioned here that in each of the two polarization state imaging schemes (linear and circular), various sub-imaging strategies have also been investigated [44,45]. These include the co-polarized imaging, the polarization difference (or subtraction) imaging and the degree of polarization (DOP) imaging. As is obvious from the nomenclature, while in the co-polarized imaging strategy, images are recorded with the same orientation of the polarizer and the analyzer (either linear or circular, $I_{\rm co}$), in the polarization difference imaging one obtains the final image by subtracting the cross-polarized image from the co-polarized image ($I_{\rm co} - I_{\rm cross}$). The relative efficacies of these different strategies have been summarized by Morgan et al. [47].

The inferences made above do not apparently seem to be encouraging for polarized light imaging of actual tissues because tissues generally have large value of anisotropy parameter ($g \sim 0.8$–0.95 [28]). However, studies carried out by Sankaran et al. to compare polarized light propagation in actual tissues (porcine adipose, arterial and myocardial tissue) and common tissue phantoms (suspension of Intralipid ® – 20% and polystyrene microsphere of 1.072 μm diameter in water) yielded very intriguing differences [18,19]. For comparable values for g and τ, depolarization of both linear and circularly polarized light was considerably more in tissue than in tissue phantoms [18,19]. More importantly, despite having large value of g (∼0.9) linearly polarized light survived through longer propagation distances than circularly polarized light in actual tissue, a behavior that was in sharp contrast to that observed for tissue phantoms. Although several other factors like the presence of a higher density [19] and a much wider distribution in the size [22] of tissue scatterers may also contribute, a much lower value of the refractive index of tissue scatterers ($n_s \sim 1.37$–1.41) as compared to those of the scatterers of the commonly used tissue phantoms ($n_s \sim 1.5$–1.6) has been identified as the major factor contributing to this discrepancy [20,21]. In fact, it has been shown that despite having large value of g, the depolarization characteristics of weakly fluctuating [low value of the relative refractive index m $(= n_s/n_m) \sim 1.03$–1.05] random medium can be similar to those of Rayleigh scatterers [14,20,21]. This is illustrated in Figure 6, where the experimentally measured degrees of linear and circular polarization from samples prepared using aqueous suspension of 0.65 μm diameter polystyrene ($n_s = 1.59$, $m = 1.2$, $g = 0.86$, $X = 4.29$) and silica microspheres ($n_s = 1.37$, $m = 1.03$, $g = 0.89$, $X = 4.29$) are displayed. Despite having a larger value for g, both linearly and circularly polarized light are observed to get depolarized much faster for the samples having silica microspheres as compared to those having polystyrene microspheres as scatterers. Interestingly, for the silica microspheres samples having $g = 0.89$, circular polarization decays faster as compared to linear polarization, a feature that is characteristic of scattering samples with small g ($\leq$0.2). Further, the dependence of depolarization on optical thickness for the samples with large sized silica microspheres is similar to that observed for samples with much smaller sized

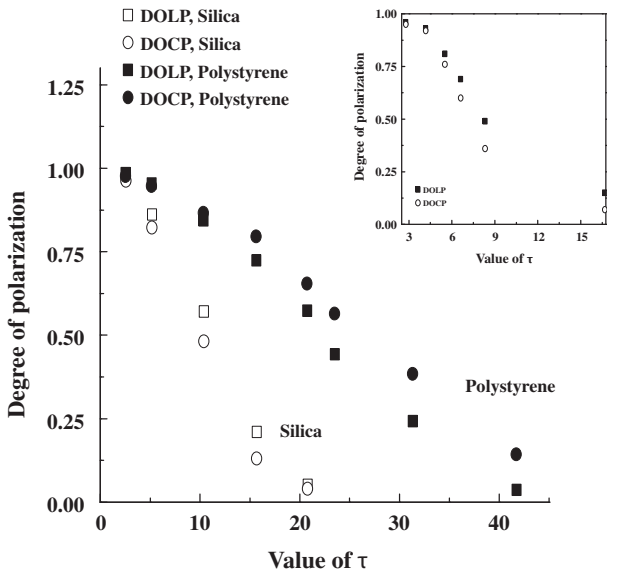

Fig. 6. Experimentally measured degrees of linear (D_{OLP}, □ and ■) and circular (D_{OCP}, ○ and ●) polarization as a function of optical thickness τ from samples prepared using aqueous (refractive index $n_m = 1.33$) suspension of 0.6 μm diameter polystyrene ($n_s = 1.59, m = 1.2, g = 0.86, X = 4.29$, solid symbols) and silica microspheres ($n_s = 1.37, m = 1.03, g = 0.89, X = 4.29$, open symbols) as scatterers. For the sake of comparison, the results for 0.11 μm diameter polystyrene microspheres ($g = 0.09, X = 0.72$) are shown in the inset. (Adapted from Ref. [21]).

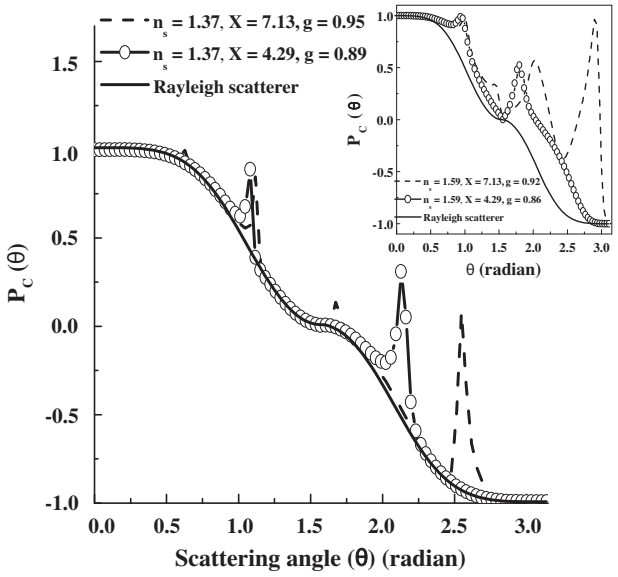

Fig. 7. The computed value of the degree of circular polarization $[P_C(\theta)]$ as a function of scattering angle after individual scattering events for scatterers with two different sizes (diameter = 0.65 μm, $X = 4.29$; and diameter = 1.08 μm, $X = 7.13$) but having the same value of refractive index $n_s = 1.37$. The variation of $P_C(\theta)$ for a Rayleigh scatterer is displayed by solid line. The inset shows the variation of $P_C(q)$ for the scatterers having the same size but with $n_s = 1.59$. (Adapted from Ref. [21].)

polystyrene microspheres (diameter = 0.11 μm, $g = 0.09$, $X = 0.72$, shown in the inset of the figure). For the two scatterers, the value of τ where degree of polarization reduces to less than 0.1 is comparable.

This anomalous depolarization behavior was found to arise due to the retention of dipolar nature of scattering in anisotropic scattering medium ($g \geq 0.7$), comprised of scatterers having a lower value of relative refractive index m $[(m-1) \ll 1, (m-1)X \ll 1]$ [20,21]. This can be understood from Figure 7, where the computed (using Eq. (15) of Sect. 3.3.1) value of the degree of circular polarization $[P_C(\theta)]$ as a function of scattering angle after individual scattering events for scatterers with two different sizes (diameter = 0.65 μm, $X = 4.29$; and diameter = 1.08 μm, $X = 7.13$) but having the same value of refractive index $n_s = 1.37$ is displayed [21]. The inset shows the variation of $P_C(\theta)$ for the scatterers having the same size but with $n_s = 1.59$. For the scatterers with $n_s = 1.59$, one obtains the expected result that is with increasing size of the scatterer, the degree of polarization is preserved up to a larger value of θ. In contrast, for the scatterers with $n_s = 1.37$, depolarization behavior does not show significant dependence on the size of the scatterer and the angular variation of degree of polarization remains much closer to that of a Rayleigh scatterer (displayed by solid lines in the figures). Further, for the anisotropic scatterers having $n_s = 1.59$, one observes flipping of helicity of incident circularly polarized light at much larger scattering angle (θ) as compared to that for Rayleigh scatterers. In contrast, for the anisotropic scatterers having $n_s = 1.37$, helicity flipping occurs at $\theta \sim 90°$ like the case for ideal dipole scattering (Rayleigh scatterer). This behavior originates from the fact that the anisotropic scatterers having a lower value of relative refractive index can be treated to be in the weak scattering regime, where each volume element inside the scatterer can be assumed to be giving electrical dipole scattering in an independent manner. The retention of this dipolar behavior leads to depolarization characteristics of such weakly fluctuating anisotropic scattering medium much similar to that of Rayleigh scatterers [21].

Numerical simulations of polarized light transport in continuous weakly fluctuating random medium carried out by Moscoso et al. [14] and Kim and Moscoso [13] also yielded similar results. Their results also indicated that polarized light imaging through biological tissue is far more attractive than the results from commonly used tissue phantoms prepared using large sized Mie scatterers would predict. In weakly fluctuating random medium like tissue, polarization can thus be used as an efficient scheme for discriminating ballistic and snake photons from diffusive photons, thus yielding less blurred images compared to polarization-blind methods.

5.2 Polarized light imaging of tissue

Based on the gained insight into depolarization properties of multiply scattered light in tissue simulating

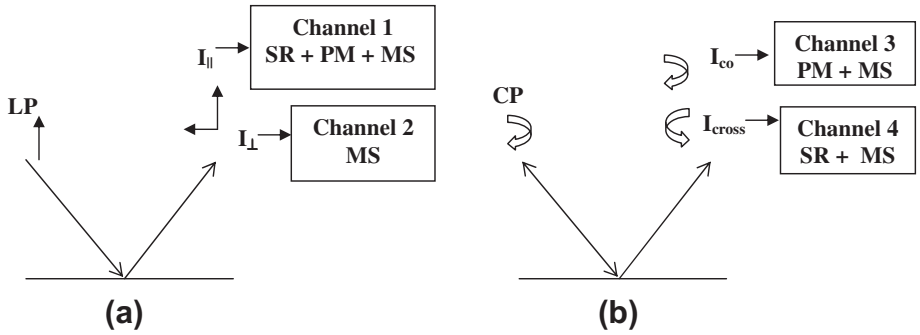

Fig. 8. Polarization discrimination detection scheme for extraction of the weakly scattered photons from superficial tissue layer by simultaneously rejecting the surface reflections and the multiply scattered photons. The left panel (a) corresponds to linear polarization illumination, co ($I_{\perp}$) and crossed-polarized ($I_{\parallel}$) detection. The right panel (b) corresponds to circular polarization illumination, co ($I_{\rm co}$) and crossed-polarized ($I_{\rm cross}$) detection. The polarization imaging scheme is $I_{\rm co} - I_{\perp} = {\rm PM}$. LP: linear polarization, CP: circular polarization, SR: Specular reflection, PM: Polarization maintaining and MS: Multiple scattered. (Adapted from Ref. [51].)

phantoms and in actual tissues, several research groups have explored polarization gating for imaging of tissue and its underlying structures [49–52]. Various polarization gating schemes and imaging strategies have been investigated for this purpose. Studies in this direction have been pioneered by Jacques et al. [49]. They demonstrated the use of a linear polarization gating scheme for imaging of the texture of the superficial (sub-surface) skin structures. In this approach, a glass plate kept in contact with the skin was optically coupled to the skin by a drop of water or other index matching liquid. The linear polarization illumination was delivered from an angle such that glare from the air/glass/skin interfaces is directed away and the viewing camera collects light that has been scattered from the interior of skin. Images in the backscattering direction were recorded with the analyzer axis oriented either parallel ($I_{\rm co}$) or perpendicular ($I_{\rm cross}$) to the illumination polarizer axis. As described previously, the polarization difference scheme ($I_{\rm co} - I_{\rm cross}$) or the degree of polarization scheme [$D_{OP} = \frac{(I_{\rm co}-I_{\rm cross})}{(I_{\rm co}+I_{\rm cross})}$] was employed to filter out the multiply scattered (image blurring) photons. The underlying principle for either of these schemes is that the multiply scattered photons emitting from deeper tissue layer are depolarized to a large extent and contribute equally to the recorded intensities in both the co-polarized and cross-polarized channels. This contribution can thus be filtered out by subtracting the image recorded using the cross-polarized channel from that recorded using the co-polarized channel. Their results also illustrated the fact that DOP imaging has subtle advantages over the polarization difference imaging [46,47]. Since the DOP image is formed by the ratio of the numerator that is primarily comprised of superficial subsurface reflectance and the denominator that is representative of total subsurface reflectance, it is insensitive to any spatial variation of illuminating light and variations in surface pigmentations (melanin pigmentations such as freckles or age marks, etc.). Based on this principle Jacques et al. also developed a polarized light camera system, which has undergone clinical trial for imaging various types of skin pathologies [50].

Morgan and Stockford [51] developed an elegant polarization scheme for eliminating surface reflection in backscattering imaging of superficial tissue layers. They have used a combination of images acquired using linearly and circularly polarized light to filter out simultaneously the surface reflections and the multiply scattered photons (from deeper tissue layer) and to extract the weakly scattered photons from superficial tissue layer. This polarization imaging scheme is summarized in Figure 8. As is apparent from the figure, the two polarization channels, linear polarization illumination with detection of cross-polarized light (indicated as $I_{\perp}$, channel 2) and circular polarization illumination with detection of co-polarized light (indicated as $I_{\rm co}$, channel 3), are both free from surface reflection. Subtraction of channel 2 from channel 3 ($I_{\rm co} - I_{\perp}$) thus enables one to filter out the multiply scattered photons and extract the weakly scattered photons from superficial tissue layer. This approach obviates the need for using matching fluid and optically flat plates (which are often not amenable to clinical situation) and also allows one to develop simpler polarized light imaging system employing co-axial detection. This technique thus appears to be promising for characterizing various types of skin pathologies.

Note that the polarization gated imaging techniques discussed above are particularly suitable for imaging superficial (subsurface) tissues (imaging depth ranging up to ∼300 μm) and are not applicable for deep tissue imaging. However, for many practical applications deep subsurface imaging of tissue is required. Demos et al. [52] have thus developed a methodology based on both spectral and polarization discrimination of back-scattered photons for deep subsurface imaging of tissue. This approach known as spectral polarization difference imaging (SPDI) exploits the difference in penetration depths of photons with different illuminating wavelengths in combination with polarization filtering for selectively imaging different tissue depths. In this approach, backscattering images from tissue were recorded using the cross-polarized channel (analyzer axis oriented perpendicular to illuminating

linear polarizer axis) for four different illuminating wavelengths (600 nm, 690 nm, 770 nm and 970 nm wavelengths selected from a white light source using narrow bandpass filters). The utilization of different illuminating wavelengths allowed for probing different depths in tissue owing to the progressively increasing penetration depths for photons with increasing illuminating wavelengths. Subtraction of polarization images recorded with a pair of illumination wavelengths enabled depth profiling in tissue [52].

Another important development in polarimetric tissue imaging is the orthogonal polarization spectral (OPS) imaging, originally proposed by Groner et al. [53]. The underlying principle is similar as described previously; the tissue is illuminated with linearly polarized light and the back-scattered light is detected in cross-polarization channel. Since the detected depolarized scattered light (passing through orthogonal polarizer) penetrates deeper in tissue, it effectively back-illuminates the absorbing material (e.g., blood present in tissue) in the foreground. This approach can therefore be exploited for imaging blood vessels in tissue. Indeed, such OPS imaging with appropriate choice of the illuminating wavelength (the wavelength was optimized to be 548 nm since at this wavelength the absorption due to the oxy- and deoxy-hemoglobins present in blood is equal) has been used for visualization and quantitative assessment of the blood vessels in microcirculation, in a number of diagnostic applications [54].

Apart from the illustrative examples of the polarization schemes described above, several other experimental approaches such as rotating polarizer imaging, polarization modulation techniques have also been explored for polarization gated imaging of tissue. Further, as has been discussed at the beginning, many tissue structures possess intrinsic polarization characteristics (such as linear birefringence, optical activity and dichroism) which may also serve as intrinsic contrast mechanisms in polarization imaging. A number of studies have therefore addressed exploring this possibility by recording complete 4×4 (16 element) Mueller matrix images of tissue.

Several researchers have also attempted combining the polarization gating technique with other ballistic light imaging modalities such as time gating and spatial filtering [7,46]. Scanning laser confocal polarimetry is one such novel approach that integrates confocal and polarimetry imaging methods, and has found widespread applications in ophthalmology [55]. Polarization-sensitive optical coherence tomography (PS-OCT) is another polarimetric imaging method that has received particular attention and has already yielded very promising results in various diagnostic applications [7]. This approach combines the depth sectioning capability of conventional optical coherence tomography (exploiting coherence gating) with polarization resolved measurements, to yield depth resolved images of the intrinsic tissue polarimetry characteristics. For details on the various experimental approaches used in PS-OCT and their applications, the reader is referred to reference [7].

6 Polarimetric techniques for tissue diagnosis: representative results

Development of optical spectroscopic techniques for biomedical diagnosis is another area actively pursued using various approaches like fluorescence, Raman scattering and elastic scattering spectroscopy [56]. For optical diagnosis, one generally exploits the scattered (both elastically and in-elastically) or re-emitted light from tissue. The elastically scattered light from tissue contains rich morphological and functional information of potential biomedical importance. On the other hand, the in-elastically scattered (Raman scattering) and re-emitted (via, processes like fluorescence) light contain useful biochemical information on the sample that can be exploited for probing subtle biochemical changes as signature of disease progression. Polarization resolved measurements on both scattered (elastically and in-elastically) and re-emitted light provide additional diagnostic information which are otherwise hidden in polarization-blind measurements.

6.1 Polarimetric elastic scattering spectroscopy

Measurement of polarization properties of elastically scattered light from tissue has been exploited for a wide variety of diagnostic applications. For example, several studies have explored measurement of depolarization (of either linear and circularly polarized light) of scattered light from tissue for the quantification of the morphological parameters like the density, size, distribution, shape and refractive index of tissue scatterers, for their diagnostic use. The most noteworthy has been the study carried out by Backman et al. [29]. They have explored polarized light scattering spectroscopy for quantitative measurement of epithelial cellular structures as signature of pre-cancerous changes in human tissues [29]. The method comprises of excitation of tissue by polarized white light and detection of the polarized component of back-scattered light. The detection of polarized component of the back-scattered light serves as a means to extract the single scattered light from superficial epithelial cell layer from the background multiply scattered light. The singly scattered light from superficial epithelial cell layer was observed to show a fine structure component that is periodic in wavelength [29]. This fine structure component was identified as being due to light that is Mie scattered by surface epithelial cell nuclei. By analyzing the amplitude and frequency of this signal using Mie theory, the size distribution and the refractive index of the nuclei were extracted. Since, the size (and distribution) and refractive index of epithelial cell nuclei are valuable parameters for detecting pre-cancerous changes, this technique has shown promise for in situ and early diagnosis of epithelial cancer [29].

In a continuation of the polarized elastic scattering spectroscopic study, Hunter et al. [30] reported that in addition to the periodic fine structure, the residual elastic scattering signal from epithelial tissue also exhibits an inverse power-law spectral component. This was

identified to originate from the self-similar (fractal) nature of micro-scale fluctuation of local refractive index in tissue. They developed a model based on the Born approximation and von Karman (self-affine) spatial correlation of submicron tissue refractive index to account for the inverse power-law variation of wavelength dependent elastic scattering signal [30]. The developed model was fitted iteratively with the measured wavelength variation of polarized scattered light intensity to obtain quantitative micro-optical parameters of tissue, namely, the fractal-Born spectral component (α), the fractal dimension (D_f) and the fractal upper scale (L). Significant differences were observed in the value of these parameters for normal and dysplastic (epithelial pre-cancer) tissues [30]. These results indicated that changes in tissue self-affinity probed via, polarized light scattering spectroscopy can serve as a potential biomarker for pre-cancer.

6.2 Polarized fluorescence spectroscopy

Among the various optical spectroscopic approaches, fluorescence spectroscopy has been particularly investigated for the diagnosis of cancer [56]. The differences in static fluorescence spectra and the differences in lifetimes of fluorescence of the endogenous tissue fluorophores both can be exploited for tissue diagnosis [56,57]. Studies carried out by us have shown that measurement on polarization (or depolarization) properties of fluorescence has several important advantages over the conventional unpolarized fluorescence measurements for cancer diagnosis [58–60]. The results of these studies revealed an interesting dependence of fluorescence polarization anisotropy (the ratio of the polarized fluorescence component to the total intensity) on tissue thickness [60]. For thin tissue sections ($t \ll l_t \sim 30\,\mu$m, l_t the transport mean free path) the polarization anisotropy values were found to be lower for normal tissues as compared to the corresponding malignant tissues and the reverse behavior was observed for thicker tissues ($t \geq l_t$, $\sim$1 mm). A phenomenological model based on diffusion approximation of light transport was developed to comprehend this observation [60,61]. This analysis suggested that the reduced polarization anisotropy (stronger depolarization) of malignant tissues for larger thickness arises due to larger multiple scattering (higher value for scattering coefficient μ_s) in malignant tissues compared to normal. This is illustrated in Figure 9, where the variation of the values for polarization anisotropy of 440 nm fluorescence (with 340 nm excitation) from malignant and normal breast tissues as a function of tissue thickness is displayed [60]. The theoretical fits with the diffusion theory-based model are also shown in the figure. These results suggested that in bulk tissues, depolarization of fluorescence due to multiple scattering dominates over other causes of depolarization fluorescence (like rotational diffusion of fluorophore and the radiationless energy transfer among fluorophores). This has interesting consequences for fluorescence-based diagnosis of cancer, as described below.

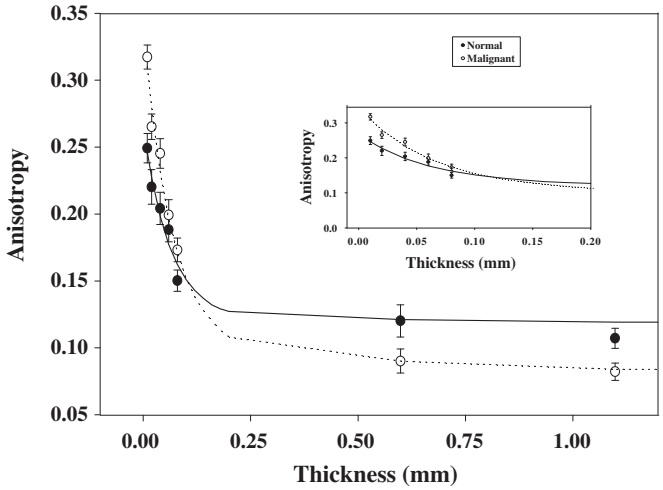

Fig. 9. Variation of the values for fluorescence polarization anisotropy of 440 nm fluorescence from malignant (○) and normal (●) breast tissues as a function of tissue thickness. The excitation wavelength used was 340 nm. The solid and dashed line profiles show theoretical fits for normal and malignant tissues respectively. An expanded view of the dependence of the anisotropy on tissue thickness for thickness less than 0.1 mm is shown in the inset. The estimated values (from the theoretical fit) for scattering coefficient m_s for normal and malignant breast tissues were 23 mm^{-1} and 29 mm^{-1} respectively. (Adapted from Ref. [60].)

Despite the early promise for diagnosis of cancer, quantitative evaluation of the biochemical basis of the disease using static fluorescence measurements alone has been rather intricate [56,57]. In a complex random medium like tissue, numerous complexities due to multiple scattering and simultaneous presences of various fluorescent and absorbing species present formidable challenges, in terms of interpretation of the underlying biochemical features. Specifically, the intrinsic fluorescence spectra of fluorophores from an optically turbid and absorbing medium as the tissue gets strongly modulated by the wavelength dependent medium absorption and scattering properties. This also leads to a large variability in both intensity and line shape (mainly originating due to an inhomogeneous distribution of absorbers and scatterers) in the static fluorescence spectra of sites belonging to the same class (normal or cancerous). Moreover, fluorescence signal from layered epithelial tissues (most cancer originates from epithelial layer), detected with conventional measurement techniques, is due to contributions from different fluorophores (having different quantum yield and spectral line shape) present in the superficial epithelial layer and the underlying connective tissue layer (stroma). In fact, the fluorescence contrast from cancerous and non-cancerous sites is known to depend on the differences in depth distribution of endogenous fluorophores in the two layers. Our studies have demonstrated that the polarization resolved measurements of fluorescence can potentially impact some of these important unresolved issues in fluorescence-based diagnosis of cancer [58,59].

Studies conducted by us on appropriately designed tissue phantoms showed that the polarized fraction of total fluorescence records only fluorescence contributions, which have not undergone significant scattering, and has therefore not traveled beyond a few transport lengths in the turbid medium [58,59]. This therefore bears lesser modulation of wavelength dependent absorption and scattering properties and is least affected by an inhomogeneous distribution of absorbers and scatterers in tissue. The reduced effect of the absorption and scattering properties of tissue on polarized fluorescence also leads to a reduced site-to-site variability (from the same tissue category) in intensity and line shape of polarized fluorescence as compared to unpolarized fluorescence [59]. Further, since multiple scattering is the dominant cause of depolarization in tissue, the fluorescence from superficial layer of tissue is the least depolarized and that originating from deeper layers becomes increasingly more depolarized. This dependence was exploited for depth resolved fluorescence measurements in tissue [58]. In this approach, measurement of fluorescence polarized at varying angles ($\Delta\theta$) with respect to excitation linear polarization was used to probe fluorophores located at different depths inside tissue. This is demonstrated in Figure 10 [58]. The polarized component of fluorescence (with 340 nm excitation) shows a prominent peak around 440 nm that arises mainly from reduced form of nicotinamide adenine dinucleotide (NADH) present in the superficial epithelial layer of tissue. For fluorescence spectra recorded at larger $\Delta\theta$, the deeper connective tissue layer (stroma) is probed. The corresponding spectra show strong signature of collagen and elastin (characteristic peak at ~400 nm [50,51]) present in that layer. Note that polarized fluorescence spectra (recorded at varying $\Delta\theta$) shown in the figure were normalized by the corresponding elastic scattering spectra recorded under the same condition. This normalization was carried out to compensate for the propagation losses of fluorescence, with the assumption that for the same wavelength λ, the elastically scattered photons suffer similar propagation losses as fluorescence photons [58]. A similar approach has also been used by Biswal et al. [62], who demonstrated that the intrinsic fluorescence spectra from a turbid medium can be recovered (removing the wavelength dependent modulation of medium absorption and scattering properties) by normalizing the polarized fluorescence spectra by the polarized elastic scattering spectra. It thus appears that polarized fluorescence measurements can be used to extract intrinsic fluorescence signature of the endogenous tissue fluorophores and can also be exploited to decouple, isolate and quantify the epithelial and stromal contribution of fluorescence which should improve the diagnostic efficiency of the fluorescence-based technique [58,59]. Note that similar strategy on polarization resolved measurements has also been exploited for depth resolved Raman spectroscopic measurements in layered epithelial tissues [63].

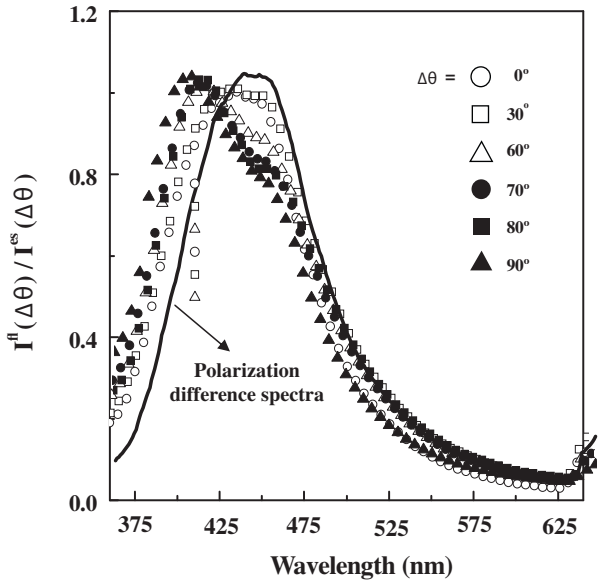

Fig. 10. The elastic scattering normalized fluorescence spectra $[I_n^{fl}(\Delta\theta,\lambda) = I^{fl}(\Delta\theta,\lambda)/I^{es}(\Delta\theta,\lambda)]$ recorded at varying angles ($\Delta\theta$) with respect to excitation linear polarization from a mice oral tissue sample. The polarization difference spectra $[I_n^{fl}(\Delta\theta = 0°,\lambda) - I_n^{fl}(\Delta\theta = 90°,\lambda)]$ are displayed by solid line. The values for m_s, m_a and g at 440 nm for this tissue were (20 mm^{-1}, 0.3 mm^{-1} and 0.88). (Adapted from Ref. [58].)

6.3 Quantitative Mueller matrix polarimetry applied to biomedical diagnosis

As noted previously, in addition to depolarization properties, many constituents of tissue exhibit intrinsic polarization characteristics of potential biomedical importance. These include linear birefringence (arising from anisotropic tissue structures; collagen, elastin and other fibrous structures), optical activity (due to presence of chiral molecules such as glucose) and dichroism (due to amino acids, proteins, nucleic acids, etc.). Each of these, if separately extracted and quantified, holds promise as a useful biological metric. Several studies have therefore addressed birefringence measurement for the detection of tissue abnormalities such as osteoarthritis, thermal injury (burns), and the numerous types of carcinomas (like basal cell, squamous cell carcinoma) [8,9,64,65]. The prospect of non-invasive glucose detection via turbid polarimetry is also being evaluated by several groups [9,34]. Earlier attempts in this direction have mainly employed semi-empirical formulations by selectively picking up appropriate matrix elements (or a combination of elements) for isolating and quantifying the polarization characteristics arising from different tissue structures. Recent studies have explored more general polarimetry analysis models for extraction, quantification and interpretation of the intrinsic tissue polarimetry characteristics. Specifically, measurement of

complete (16) Mueller matrix elements and their analysis through different decomposition methods have been explored for this purpose [33]. For recording Mueller matrix from tissue, various experimental strategies described in Section 4 (either using the dc measurement approaches or using the polarization modulation-synchronous detection schemes) have been employed. Various decomposition algorithms have also been developed for polarimetry analysis.

Mueller matrix decomposition consists of decomposing a 'lumped' system Mueller matrix $\mathbf{M}$ into the product of three '*basis*' matrices [27]

$$\mathbf{M} = \mathbf{M}_{\Delta} \cdot \mathbf{M}_{R} \cdot \mathbf{M}_{D},$$

where $\mathbf{M}_{\Delta}$ accounts for the depolarizing effects of the medium, $\mathbf{M}_{R}$ describes the effects of linear and circular retardance, and $\mathbf{M}_{D}$ includes the effects of linear and circular diattenuation (or dichroism). This particular type of product decomposition was originally proposed by Lu and Chipman for optically clear media [27]. This decomposition is a particular case among the six possible product decompositions (based on the multiplication order of the three constituent *basis* matrices). In fact, algorithm for decomposing with multiplication order of the *basis* matrices reverse to that of the Lu-Chipman decomposition has also been developed ($\mathbf{M} = \mathbf{M}_{D} \cdot \mathbf{M}_{R} \cdot \mathbf{M}_{\Delta}$, known as the *reverse* decomposition) [66]. It has been shown that the other possible decompositions can be obtained from these two decompositions by using similarity transformations [66]. While, these two decomposition processes have been the most widely explored for analyzing tissue polarimetry signal, few other types of decomposition processes have also been proposed [67,68]. These include the *symmetric* decomposition developed by Ossikovski [67] and the sum decomposition, known as the *Cloude* decomposition [68]. Nevertheless, once decomposed, the constituent 'basis' matrices are further analyzed to derive individual polarization medium properties, namely, linear retardance (δ, and its orientation angle θ), optical rotation (ψ), diattenuation (d) and depolarization coefficient (Δ) [33].

Ghosh et al. (the lead author of this paper was also part of these studies) have performed comprehensive validation of the Mueller matrix decomposition approaches to delineate individual intrinsic polarimetry characteristics in complex turbid media such as tissues [33]. Experimental validation was performed on optical phantoms having controlled sample polarizing properties [69]. Additional theoretical validation tests were also performed on Monte Carlo-generated Mueller matrices [70]. Following successful validation, this approach was explored for monitoring of myocardial tissue regeneration following stem cell therapy (through linear birefringence measurement and quantification) with early indications showing promise for polarized light monitoring of regenerative treatment of heart [71]. Initial studies on the use of this approach for quantification of optical rotation caused by chiral molecules in turbid medium (like, for example, glucose in human tissue) have also yielded very encouraging results [71]. The first in vivo use of the Mueller matrix decomposition method for tissue structural anisotropy measurement was also demonstrated by this group using a dorsal skin-fold window chamber mouse model [72].

Chung et al. [64], Manhas et al. [73] and Anastasiadou et al. [74] have explored the use of the Mueller matrix decomposition approach for diagnosis of oral cancer and cervical cancer respectively. Interesting differences have been reported by them in the Mueller matrix-decomposed values for linear retardance (δ) and depolarization coefficient (Δ) for the cancerous and the normal tissues, indicating the potential of Mueller matrix polarimetry for non-invasive and early diagnosis of cancer. The recent studies of Pierangelo et al. on exploring the use of multi-wavelength Mueller matrix imaging for early diagnosis of colon cancer have also yielded very promising results [75,76]. Clearly, there are many other potential applications of Mueller matrix polarimetry, both in tissue diagnostics and in treatment response monitoring.

7 Concluding remarks

In this paper, the use of turbid medium polarimetry for biomedical applications has been reviewed. As is apparent, turbid polarimetry research has two major directions: (i) polarization can be used as a gating mechanism for imaging through tissue, and (ii) the intrinsic tissue polarimetry characteristics contain useful morphological, biochemical and functional information that can be exploited for non-invasive, quantitative tissue diagnosis and for treatment or prognosis assessment. For either of these applications, accurate measurement of the polarization-retaining signal, forward modeling of complex tissue polarimetry events and inverse analysis for separating out the constituent contributions from simultaneous scattering and polarization effects are extremely important. Despite the inherent difficulty of polarimetric approach for examinations of complex turbid media such as tissue, significant progress has been made toward performing reliable measurements and analyses. A variety of experimental and theoretical tools have been developed to maximize measurement sensitivity, interpret the measurement results, isolate specific polarization contributions of interest and evaluate the validity of polarimetry for tissue examination. These have been illustrated in this paper with representative results. The next step is obviously to use these promising polarimetric techniques in clinical settings, which is currently being rigorously investigated. Specifically, the initial in vivo biomedical deployments of polarization gated imaging and spectroscopy, which are based on relatively simpler polarization measurement schemes (such as co-polarization and crossed-polarization detection), have already shown promise. However, clinical applications of the intrinsic tissue polarimetry characteristics, e.g., for non-invasive glucose monitoring and for in situ quantification of tissue structural anisotropy, are yet to be accomplished. Since any such attempt involves more complex measurement strategies (such as recording the 16 element Mueller

matrix), one will have to deal with the challenges posed by the in vivo measurement difficulties, the confounding effects of the scattering/detection geometry, in addition to the formidable biological complexity inherent in the clinical problems. Current research is thus directed toward developing clinically amenable measurement methods for in vivo determination of the geometry-independent metrics of tissue polarimetry characteristics, for their potential applications in tissue diagnostics and in treatment response monitoring. Nevertheless, the turbid polarimetry progress to date bodes well for future in vivo developments. Finally, it may come to pass that the solutions for many clinical problems lie in combining polarimetry with other optical (spectroscopic) methods, judiciously combining their complementary strengths for non-invasive optical diagnostics and imaging.

References

1. V. Ronchi, *The Nature of Light* (Harvard University Press, Cambridge, Massachusetts, 1970)
2. J. Michl, E.W. Thulstrup, *Spectroscopy with Polarized Light* (VCH, New York, 1986)
3. D.S. Kliger, J.W. Lewis, C.E. Randall, *Polarized Light in Optics and Spectroscopy* (Academic Press–Harcourt Brace Jovanovich, New York, 1990)
4. L.V. Wang, G.L. Coté, S.L. Jacques, J. Biomed. Opt. **7**, 278 (2002)
5. V.V. Tuchin, L. Wang, D.A. Zimnyakov, *Optical Polarization in Biomedical Applications* (Springer-Verlag, Heidelberg, 2006)
6. J.M. Schmitt, A.H. Gandjbakhche, R.F. Bonner, Appl. Opt. **31**, 6535 (1992)
7. J.F. de Boer, T.E. Milner, J. Biomed. Opt. **7**, 359 (2002)
8. P.J. Wu, J.T. Walsh Jr., J. Biomed. Opt. **11**, 014031 (2006)
9. R.J. Mc Nichols, G.L. Cote, J. Biomed. Opt. **5**, 5 (2000)
10. C. Brosseau, *Fundamentals of Polarized Light: A Statistical Optics Approach* (Wiley, New York, 1998)
11. D. Bicout, C. Brosseau, A.S. Martinez, J.M. Schmitt, Phys. Rev. E **49**, 1767 (1994)
12. E.E. Gorodnichev, A.I. Kuzolov, D.B. Rozozkin, JETP Lett. **68**, 22 (1998)
13. A.D. Kim, M. Moscoso, Phys. Rev. E **64**, 026612 (2001)
14. M. Moscoso, J.B. Keller, G. Papanicolaou, J. Opt. Soc. Am. A **18**, 948 (2001)
15. L.F. Rojas-Ochoa et al., J. Opt. Soc. Am. A **21**, 1799 (2004)
16. L. Wang, S.L. Jacques, L. Zheng, Comput. Meth. Programs Biomed. **47**, 131 (1995)
17. M.F.G. Wood, X. Guo, I.A. Vitkin, J. Biomed. Opt. **12**, 014029 (2007)
18. V. Sankaran, K. Schonenberger, J.T. Walsh Jr., D.J. Maitland, Appl. Opt. **38**, 4252 (1999)
19. V. Sankaran, J.T. Walsh Jr., D.J. Maitland, J. Biomed. Opt. **7**, 300 (2002)
20. N. Ghosh, A. Pradhan, P.K. Gupta, S. Gupta, V. Jaiswal, R.P. Singh, Phys. Rev. E **70**, 066607 (2004)
21. N. Ghosh, P.K. Gupta, A. Pradhan, S.K. Majumder, Phys. Lett. A **354**, 236 (2006)
22. N. Ghosh, H.S. Patel, P.K. Gupta, Opt. Express **11**, 2198 (2003)
23. E. Collette, *Polarized Light: Fundamentals and Applications* (Marcel Dekker Inc., New York, 1990)
24. C.F. Bohren, D.R. Huffman, *Absorption and Scattering of Light by Small Particles* (Wiley, New York, 1983)
25. W.S. Bickel, W.M. Bailey, Am. J. Phys. **53**, 468 (1985)
26. R.A. Chipman, *Handbook of Optics*, edited by M. Bass, 2nd edn., Vol. 2 (McGraw-Hill, New York, 1994)
27. S.Y. Lu, R.A. Chipman, J. Opt. Soc. Am. A **13**, 1106 (1996)
28. A.J. Welch, M.J.C. Van Germert, W.M. Star, B.C. Wilson, in *Optical Thermal Response of Laser Irradiated Tissue*, edited by A.J. Welch, M.J.C. Van Germert (Plenum, New York, 1995)
29. V. Backman et al., Nature (London) **406**, 35 (2000)
30. M. Hunter et al., Phys. Rev. Lett. **97**, 138102 (2006)
31. N. Ghosh, P. Buddhiwant, A. Uppal, S.K. Majumder, H.S. Patel, P.K. Gupta, Appl. Phys. Lett. **88**, 084101 (2006)
32. A. Ishimaru, *Wave Propagation and Scattering in Random Media* (Academic Press, New York, 1978)
33. N. Ghosh, M. Wood, I.A. Vitkin, *Handbook of Photonics for Biomedical Science*, edited by V.V. Tuchin (CRC Press, Taylor and Francis Group, London, 2010), Chap. 9
34. M.F.G. Wood, N. Ghosh, X. Guo, I.A. Vitkin, *Handbook of Optical Sensing of Glucose in Biological Fluids and Tissues*, edited by V.V. Tuchin (Taylor & Francis Publishing, 2008), Chap. 17
35. M. Xu, R.R. Alfano, Phys. Rev. Lett. **95**, 213901 (2005)
36. D.A. Zymniakov, Y.P. Sinichkin, P.V. Zakharov, D.N. Agafonov, Waves Random Media **11**, 395 (2001)
37. E. Collett, Opt. Commun. **52**, 77 (1984)
38. M. Mujat, A. Dogariu, Appl. Opt. **40**, 34 (2001)
39. X. Guo, M.F.G. Wood, I.A. Vitkin, J. Biomed. Opt. **11**, 041105 (2006)
40. J.S. Baba, J.R. Chung, A.H. DeLaughter, B.D. Cameron, G.L. Cote, J. Biomed. Opt. **7**, 341 (2002)
41. R.M.A. Azzam, Opt. Lett. **2**, 148 (1978)
42. D.H. Goldstein, Appl. Opt. **31**, 6676 (1990)
43. A. De Martino, E. Garcia-Caurel, B. Laude, B. Drévillon, Thin Solid Films **120**, 455 (2004)
44. B. Laude-Boulesteix, A. De Martino, B. Drévillon, L. Schwartz, Appl. Opt. **43**, 2824 (2004)
45. M. Dubreuil, S. Rivet, B. Le Jeune, J. Cariou, Opt. Express **15**, 13660 (2007)
46. J.C. Hebden, S.R. Arridge, D.T. Delpy, Phys. Med. Biol. **42**, 825 (1997)
47. S.P. Morgan, M.P. Khong, M.G. Somekh, Appl. Opt. **36**, 1560 (1997)
48. S.P. Schilders, X.S. Gan, M. Gu, Appl. Opt. **37**, 4300 (1998)
49. S.L. Jacques, J.R. Roman, K. Lee, Lasers Surg. Med. **26**, 119 (2000)
50. S.L. Jacques, R.J. Roman, K. Lee, J. Biomed. Opt. **7**, 329 (2002)
51. S.P. Morgan, I.M. Stockford, Opt. Lett. **28**, 114 (2003)
52. S.G. Demos, H.B. Radousky, R.R. Alfano, Opt. Express **7**, 23 (2000)
53. W. Groner et al., Nat Med. **5**, 1209 (1999)
54. V. Cerny, Z. Turek, R. Parizkova, Physiol. Res. **56**, 141 (2007)
55. F. Ferreri, P. Aragona, G. Ferreri, Prog. Brain Res. **173**, 125 (2008)

56. N. Ramanujam, Neoplasia **2**, 1 (2000)
57. R. Richards Kortum, E. Servick-Muraca, Annu. Rev. Phys. Chem. **47**, 556 (1996)
58. N. Ghosh, S.K. Majumder, H.S. Patel, P.K. Gupta, Opt. Lett. **30**, 162 (2005)
59. N. Ghosh, S.K. Majumder, P.K. Gupta, Opt. Lett. **27**, 2007 (2002)
60. S.K. Mohanty, N. Ghosh, S.K. Majumder, P.K. Gupta, Appl. Opt. **40**, 1147 (2001)
61. N. Ghosh, S.K. Majumder, P.K. Gupta, Phys. Rev. E **65**, 26608 (2002)
62. N.C. Biswal, S. Gupta, N. Ghosh, A. Pradhan, Opt. Express **11**, 3320 (2003)
63. Z.J. Smith, A.J. Berger, Opt. Lett. **30**, 1363 (2005)
64. J. Chung et al., Appl. Opt. **46**, 3038 (2007)
65. K. Schoenenberger, B.W. Colston Jr., D.J. Maitland, L.B. Da Silva, M.J. Everett, Appl. Opt. **37**, 6026 (1998)
66. R. Ossikovski, A. De Martino, S. Guyot, Opt. Lett. **32**, 689 (2007)
67. R. Ossikovski, J. Opt. Soc. Am. A **26**, 1109 (2009)
68. R. Ossikovski et al., Phys. Stat. Sol. (a) **205**, 720 (2008)
69. N. Ghosh, M.F.G. Wood, I.A. Vitkin, J. Biomed. Opt. **13**, 044036 (2008)
70. N. Ghosh, M.F.G. Wood, I.A. Vitkin, J. Appl. Phys. **105**, 102023 (2009)
71. N. Ghosh, M.F.G. Wood, S.-H. Li, R.D. Weisel, B.C. Wilson, R.-K. Li, I.A. Vitkin, J. Biophoton. **2**, 145 (2009)
72. M.F.G. Wood, N. Ghosh, E.H. Moriyama, B.C. Wilson, I.A. Vitkin, J. Biomed. Opt. **14**, 014029 (2009)
73. S. Manhas, M.K. Swami, H.S. Patel, A. Uppal, N. Ghosh, P.K. Gupta, J. Biophoton. **2**, 581 (2009)
74. M. Anastasiadou et al., Phys. Stat. Sol. (c) **5**, 1423 (2008)
75. A. Pierangelo, A. Benali, M.-R. Antonelli, T. Novikova, P. Validire, B. Gayet, A. De Martino, Opt. Express **19**, 1582 (2011)
76. M.R. Antonelli, A. Pierangelo, T. Novikova, P. Validire, A. Benali, B. Gayet, A. De Martino, Opt. Express **18**, 10200 (2010)